Estuarine, Coastal and Shelf Science 288 (2023) 108350

Contents lists available at ScienceDirect

Estuarine, Coastal and Shelf Science

journal homepage: www.elsevier.com/locate/ecss

A storm driven turbidity maximum in a microtidal estuary

Matteo Postacchini [a,*], Andrew J. Manning [b,c,d,e,f], Joseph Calantoni [g], Joseph P. Smith [h], Maurizio Brocchini [a,d]

[a] Università Politecnica delle Marche, Ancona, Italy
[b] HR Wallingford, Coasts and Oceans Group, Wallingford, UK
[c] Environment and Energy Institute, University of Hull, Hull, UK
[d] University of Florida, Gainesville, FL, USA
[e] Center for Applied Coastal Research, University of Delaware, Newark, DE, 19716, USA
[f] University of Plymouth, Plymouth, Devon, UK
[g] Ocean Sciences Division, U.S. Naval Research Laboratory, Stennis Space Center, MS, USA
[h] Department of Ocean and Atmospheric Sciences, U. S. Naval Academy, Annapolis, MD, USA

ARTICLE INFO

Keywords:
Microtidal estuary
Wave–current interaction
Turbidity maxima zone
Floc dynamics
Estuarine dynamics

ABSTRACT

Many macro- and mesotidal estuaries are characterized by Turbidity Maxima Zones (TMZs), regions with suspended solid concentrations that are much higher than those found throughout the rest of the estuary. Such regions are located near the upriver limit of salt intrusion and their position and extent are modulated and driven by tidal oscillations, especially in estuaries where tidal forcing is large. Hence, pronounced TMZs are not typically expected in micro-tidal estuaries. Field experiments were carried out in the microtidal estuary of the Misa River (northeast coast of Italy) with the aim to analyze riverine-coastal ocean interactions during different climatic conditions, freshwater discharge and tidal forcing. The goal was also that of identifying factors and episodic conditions that could lead to the evolution of ephemeral TMZs in this microtidal estuarine system. Observational results, combined to a flocculation model suite, describe the hydrodynamics, morphological bed evolution, water chemistry and floc dynamics within the estuary during wintertime quiescent and stormy periods. Pronounced TMZs with different location and extent were observed during two storms with different intensities, when enhanced freshwater discharge, wave action and tidal oscillation generated significant stratification of the lower estuarine water column. Higher turbidity values were observed throughout the TMZ during the smaller/weaker storm, while stronger surface mixing during the stronger storm led to greater dispersion of the (re-)suspended particulate load throughout the upper water column, providing a less pronounced TMZ along the bed of the lower estuary. Observations in the Misa River, potentially valid for other microtidal estuaries, show that: 1) episodic storm conditions that significantly increase freshwater discharge can lead to the evolution of an ephemeral TMZ that is modulated, but not controlled, by tidal oscillations and surface mixing conditions; 2) ephemeral TMZ localization, intensity, and extent during episodic storm events is a function of storm intensity; 3) moderately enhanced freshwater flow during an episodic storm event promotes a high degree of stratification, allowing for the formation of large flocs with great settling rates, leading to a pronounced TMZ forming downriver of the landward limit of seawater intrusion; whereas higher freshwater flows during stronger storm events lead to less stratification, greater bottom turbulence and potential TMZ suppression near the riverbed, with shear conditions promoting smaller flocs with lower settling and a greater potential for suspended particulate export from the lower estuary to coastal waters.

1. Introduction

To improve the management and maximize the resilience of coastal systems, an increase in the understanding of estuarine processes, including the hydrodynamics and sediment transport in estuaries, is needed (Bertin and Olabarrieta, 2016; Melito et al., 2018). Estuarine processes differ between different estuary types, which can be defined by many factors such as geomorphology, tidal range, and mixing

* Corresponding author.
E-mail address: m.postacchini@staff.univpm.it (M. Postacchini).

https://doi.org/10.1016/j.ecss.2023.108350
Received 5 September 2022; Received in revised form 29 March 2023; Accepted 20 April 2023
Available online 26 April 2023

(Davies, 1964; Cooper, 2001). Furthermore, estuarine dynamics and circulation depends on the complex interplay between tides, wind waves, freshwater outflow, sediment transport and accumulation, and geomorphology. Full understanding of estuarine dynamics and circulation is still a challenge (Anthony, 2015; Bertin and Olabarrieta, 2016; Brocchini, 2020). Additional complexity derives from the active mixing between freshwater inflows and ocean water, leading to differing degrees of stratification and mixing, and strong spatial and temporal variations of physiochemical and chemical parameters such as turbidity, nutrient concentrations, salinity, temperature, pH, and dissolved oxygen that can in turn influence biological productivity (Pritchard, 1967; Talke et al., 2009; Geyer and MacCready, 2014).

Estuaries are often categorized as micro-, meso- and macrotidal estuaries (Davies, 1964). Microtidal estuaries (absolute tidal range <2 m and relative tidal range <3) are dominated by wind, wave forcing and freshwater inflows, but also by tidal forcing, with net circulation being a combined balance from all these variables (Monbet, 1992; Niedda and Greppi, 2007). Turbidity Maxima Zones (TMZs) are prominent features in many meso- (e.g., Tamar Estuary in UK), macro- (e.g., Gironde Estuary in France) and hyper-tidal range (e.g., Severn Estuary) estuaries. These zones are defined as regions with considerable higher suspended solid concentrations above typical background levels (Uncles et al., 1985; Dyer et al., 2002; Manning et al., 2010), primary due to enhanced sediment re-suspension related to shear along the estuarine bed (and, to a lesser extent, salinity induced flocculation) near the landward limits of salt intrusion or within the freshwater zone (Schubel, 1968; Uncles et al., 1998; Burchard et al., 2018). TMZ formation (including extent and location) is commonly attributed to mechanisms such as tidal asymmetry, and turbulence damping effects (Lin and Kuo, 2001) which all contribute to net estuarine circulation. Net estuarine circulation is the residual circulation at specific estuarine location. Prediction of net estuarine circulation has been an important challenge since the 1950's (Stommel and Farmer, 1953; Hansen and Rattray, 1965; Nunes-Vaz et al., 1990; Li and O'Donnell, 2005). Long-term mean residual circulation is a complex interplay of freshwater inputs, prevailing wind conditions, oceanic tides, local topography bathymetry, and geomorphology, and (in larger areas) Coriolis forcing related to Earth's rotation (Wijeratne and Rydberg, 2007). Sub-tidal barotropic and baroclinic motions play an important role in net estuarine circulation in deeper estuaries with moderate to high tidal ranges (Liungman et al., 2001; Souto et al., 2003).

The formation of a TMZ in estuaries with energetic tidal flows (Dyer, 1986) is governed, to a large degree, by tidal conditions and tidal asymmetry (Allen et al., 1980; Postma, 1980; Burchard et al., 2018). Tidal asymmetry is mainly related to the bathymetry and topography of an estuary, which can distort the tidal curve and lead to net transport of sediments towards the head of the estuary. This residual transport, known as tidal pumping, is more significant than residual estuarine circulation in estuaries of high tidal range, and its interaction with both sediment settling and resuspension and re-entrainment during the tidal cycle produces and maintains the TMZ. While the TMZ in macrotidal estuaries has often been attributed primarily to tidal asymmetry, with the TMZ location controlled by the tidal-pumping magnitude, some studies have emphasized the importance of both tidal asymmetry and residual circulation in controlling TMZ formation, location, intensity and extent (Allen et al., 1980; Kirby and Parker, 1982; Uncles et al., 2002).

A close-up view into a typical estuarine TMZ reveals sedimentary mixtures affected by flocculation, a process whereby cohesive and fine-grained mixed sediment particles have the potential to aggregate into flocs (Winterwerp and Van Kesteren, 2004; Mehta, 2013). Flocculated muddy sediments often significantly contribute to both the formation of concentrated near-bed suspension layers and TMZs within tidal estuarial waters (Horemans et al., 2020), thus altering turbulent mixing in the water column. Cohesive sediments that are mixed into a predominately cohesionless sandy region can create a "cage-like" structure, thereby trapping the sand within a clay-floc envelope (Whitehouse et al., 2000). The size of flocs ranges from microns to centimeters, and their settling velocity is significantly greater than the constituent particles, while their effective density generally decreases with size (Tambo and Watanabe, 1979; Spencer et al., 2010; Zhang et al., 2018). Macrofloc (diameter (D) $>$ 160 μm) are the most important sub-group of flocs, as their fast-settling velocities, typically of the order of (5–10) mm s^{-1} (Manning and Dyer, 2007; Soulsby et al., 2013), tend to have the most influence on the mass settling flux (Mehta and Lott, 1987). Further, the TMZ encompasses a zone where the physio-chemical and compositional properties of the water changes rapidly from those of fresh water to those of sea water, thus underlining the important role of the floc dynamics in the estuarine region (Dyer, 1989).

Although TMZs are typically associated with tidal forcing in meso-, macro- and hyper-tidal range (e.g., Severn Estuary) estuaries, less prominent and ephemeral, storm-induced TMZs also occur and have been documented in microtidal systems (Chen et al., 2018). These less prominent and ephemeral TMZs play an important role in determining net sediment accumulation and transport in estuarine characterized by lower tidal energy. As an example, Geyer et al. (2001) showed that net sediment transport in the micro-tidal lower Hudson River estuary is landward, from the sea into the estuary, with sediment trapping and accumulation patterns mainly controlled by the magnitude of freshwater flow in relation to the modulation effect of the tides. When the spring tide coincides with episodic high-river discharge, net sediment export from the estuary to the sea occurs (Geyer et al., 2001).

In contrast to TMZs in highly dynamic estuarine regimes with moderate to high tidal ranges, ephemeral TMZs in microtidal estuaries are less studied, especially in case of microtidal environments (MTEs) with little water exchanges between river and sea (i.e. little tidal prism) with a lower frequency of conditions that are conducive to TMZ development. The investigation on TMZ-related processes and net landward vs. sediment transport in the lower Hudson River estuary conducted by Geyer et al. (2001) was in an MTE characterized by a tide range slightly larger than 1 m, but with a quite important tidal prism.

This work presents observational data collected from the Misa River (MR hereafter) estuary, a MTE located on the northeast coast of Italy bordering the western Adriatic Sea that is characterized by little river-sea water exchange and a tidal prism of order ~(10–100) m^3 during wintertime quiescent periods, stormy, and transitional periods between storms. The data collected are used to describe the hydrodynamics, morphological bed evolution, and water physio-chemistry of the MR under these different conditions along with results of simulations of flocculation dynamics using an existing model suite. In terms of novelties and main goals, the present work aims to: 1) investigate ephemeral TMZ formation and identify conditions under which a TMZ generates in a MTE, here represented by the MR estuary; 2) identify the main contributing factors that lead to TMZ formation and influence ephemeral TMZ localization, intensity, and extent; 3) characterize ephemeral TMZ generation under different forcing conditions in terms of physio-chemical parameters and flocculation, and understand how these factors influence TMZ location, intensity, and extent and net sediment transport through the MTE.

2. Materials and methods

2.1. Field site

The MR originates in the Apennine Mountains ("Appennino umbro-marchigiano"), runs over a watershed area of ~383 km^2 for ~48 km, and flows into the northeastern Adriatic coast of Italy. The final reach passes through the municipality of Senigallia (Marche Region) and is heavily engineered, being comparable to a field-scale laboratory. The beach to the north of the estuary is protected by breakwaters, while the southern part is a natural open coast (Fig. 1).

Falling into the MTE category, the MR is such that the tidal currents

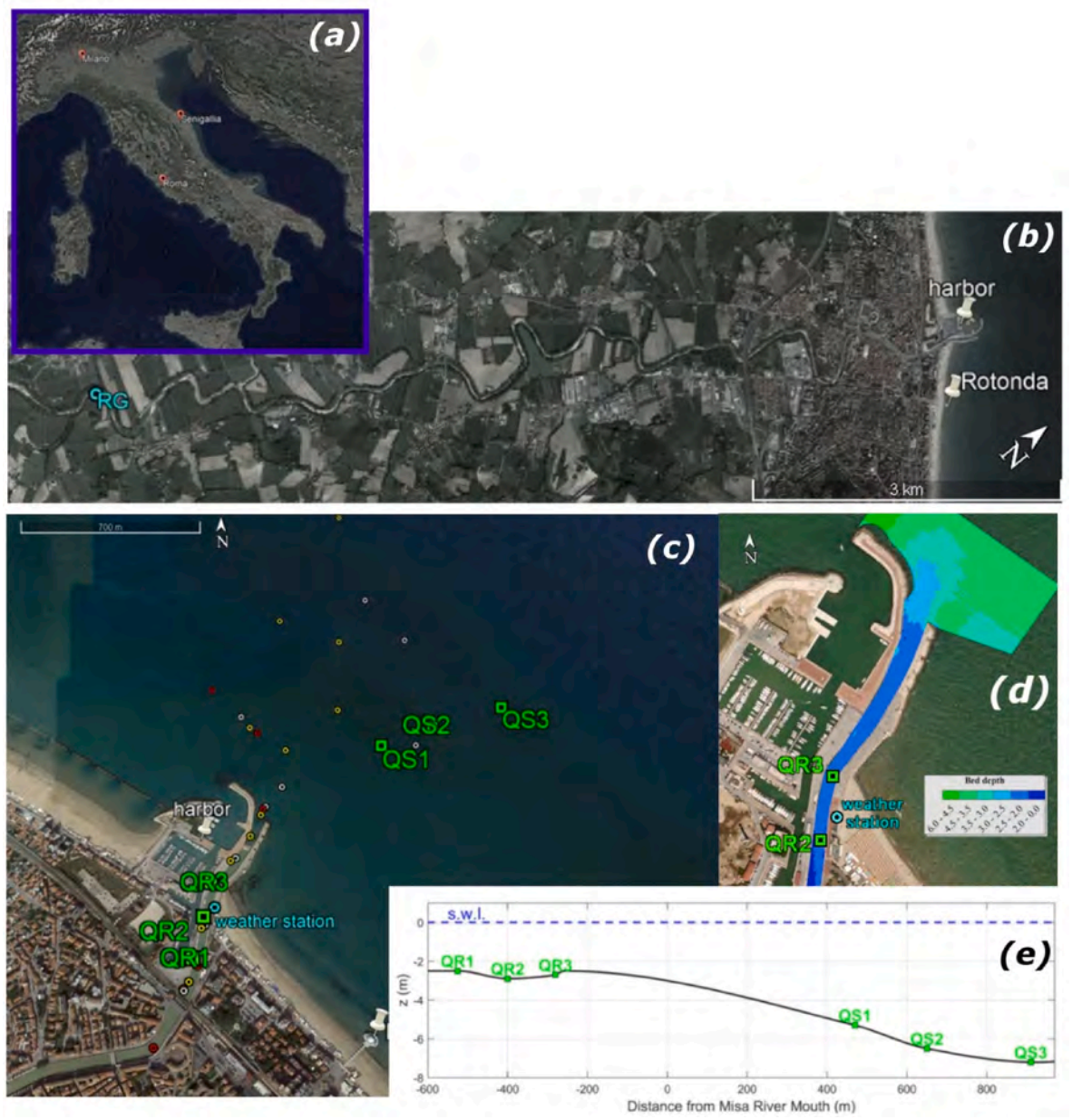

Fig. 1. (a) Italy map. (b) Location of the river gauge (RG). (c) Study area of winter experiments (Senigallia, Italy), with location of quadpods in the river (QR) and sea (QS), and sampled stations referring to 26 (white circles), 27 (yellow circles) and 29 (red circles) January 2014. (d) Bathymetric survey of the estuarine area before the experiment. (e) Bed elevation within river (negative x values) to sea (positive x values). (For interpretation of the references to color in this figure legend, the reader is referred to the Web version of this article.)

are small (Melito et al., 2020), with the tide range rarely exceeding 0.6 m. Tidal amplitudes observed in January 2014 in the port of Ancona (~25 km South of Senigallia) were ~0.25 m during neap tides and ~0.45 m during spring tides.[1] During such periods, the diurnal K1 constituent was larger than the semi-diurnal M2, with amplitudes of ~0.15 m and 0.07 m, respectively (Pawlowicz et al., 2002). The tidal excursion can reach more than 2 km inland (Brocchini et al., 2015; Postacchini et al., 2020, 2022). Similar to many Mediterranean estuaries, that of the MR is a salt-wedge estuary (Kennish, 2019) during periods of high river discharge, when the freshwater input prevails over the lower tidal forcing. During these episodic periods, a stratified gradually thinning freshwater layer flows gravitationally downriver over a seawater tongue that extends landward up the estuary. A statistical analysis of available hydrodynamic data allowed for a discharge estimate of ~400 and ~600 m^3s^{-1} for return periods of 100 and 500 years, respectively (Brocchini et al., 2017). A reduction of freshwater flow is expected for the MR in the future, due to climatic variability and human activities in Central Italy (Darvini and Memmola, 2020).

The MR contains and distributes large quantities of sediment, with the grain size at the estuary ranging from clay sizes to cobble and the fine sediments being characterized by strongly cohesive montmorillonite clay minerals (2–5 μm in size). Episodic sediment and enhanced suspended load transport from the Apennine Mountains towards the MR mouth and into the coastal western Adriatic Sea is forced by heavy rains leading to higher river discharge that typically occur as the frequency and intensity of Bora winds increase and as the temperature difference between Sirocco winds and air masses in the northern Adriatic Sea

[1] Data available at https://www.mareografico.it/.

increases (Milliman and Syvitski, 1992). The total sediment discharge from the mouth of the MR estuary is estimated to be $8.4{\cdot}10^8$ kg yr^{-1} (Frignani et al., 2005) and $4.7{\cdot}10^8$ kg yr^{-1} for the suspended load (Milliman and Syvitski, 1992). Once the Apennine river-sourced sediments discharge into the nearshore zone of the Western Adriatic, alongshore sediment transport is dominant over cross shore. Apennine river sediments are primarily transported southward by the Western Adriatic Coastal Current (WACC), enhanced by the winter Bora and during the relaxation of Sirocco winds (Fain et al., 2007; Orlic et al., 1992), while the Deep-Water Outflow Current (DWOC) transports sediments discharged by Alpine rivers through the central portion of the Adriatic Sea (Tomadin, 2000; Colantoni and Mencucci, 2010).

2.2. 2014 Field experiment

A field experiment was executed in the MR estuary in January 2014 (Fig. 1). The experiment was aimed at understanding the main estuarine processes occurring during the winter in this representative MTE by collecting hydrodynamic, morphological and physio-chemical data (for details, see Brocchini et al., 2015, 2017). To monitor the range of suspended sediment concentrations, morphodynamic and hydrodynamic, and physicochemical conditions during quiescent periods, stormy and transitional period between storms, a wide range of *in-situ* instrumentation was deployed for varying durations from the lower reach of the MR to approximately 1 km offshore of the mouth.

Due to the combined factors of deployment duration, ambient conditions expected during winter measurements, remote instrumentation recording, and minimizing the disturbance of the water column (in particular any developing interfacial gradients), the majority of the sensors were acoustic based. The hydrodynamics of the system was observed using five bottom moorings called quadpods (Fig. 2), with each of them having a dedicated instrumentation suite. Similar to recent field campaigns (e.g., Klammler et al., 2021), four large square plates of (49 $\times$ 49) cm^2 were placed at the four corners of the base to prevent the quadpods from sinking in soft sediments (mainly silt and some gravel in the final reach of the MR, fine sand in the nearshore area) and to provide a location for weights to prevent the quadpods from being disturbed or mobilized by large waves or currents. The onboard compass and constant recording of pitch and roll were also used to check eventual mobilization of the quadpods. Each quadpod covered 1 m^2 at the base and was 1 m in height.

The five quadpods were deployed at six different locations within the river, approximately in the middle of the cross-section (i.e., QR1, QR2, QR3), and in the sea (i.e., QS1, QS2, QS3), as illustrated in Fig. 1c. The use of a crane and divers allowed the quadpods to be readily moved and redeployed along the river. Specifically, two quadpods were initially deployed at QR1 (~530 m upriver of the mouth) between 22 and 24 January, and then moved to QR2 (~400 m upriver of the mouth) between 24 and 29 January. A third quadpod was deployed at QS1 (~460 m offshore, at ~5-m depth) between 23 and 27 January. The fourth quadpod was first deployed at QS2 (~640 m offshore, at ~6-m depth) between 23 and 27 January, and then moved to QR3 (~290 m upriver of the mouth) between 27 and 29 January. The fifth quadpod was constantly measuring at QS3 (~900 m offshore, at ~7-m depth) between 23 and 29 January (Fig. 1c).

Fig. 2. One of the quadpods deployed in the MR.

A bathymetric survey carried out few days before the experiment (Fig. 1d) and a long-river/cross-shore profile extracted from the instrument recordings (Fig. 1e) better show the pod locations and the bed elevation in the study area. Since the final reach of the MR is highly engineered, the cross-sections are almost rectangular and fairly uniform between QR1 and QR3 locations, their widths being ~20m. Moving downriver, the width increases, reaching almost 40m at the mouth. In terms of bed elevation, although this globally tends to decrease between QR1 and the mouth, a small bed perturbation is visible just downriver of QR3 (Fig. 1e), which gave rise to a river mouth bar in the years following the experimental campaign (Baldoni et al., 2021).

Observations made at QR2 and QS2 were used for the analysis of a big Bora storm (BS hereafter) occurring during 24–25 January 2014, while those located at QR2 and QR3 were used for the analysis of a smaller storm (SS hereafter) occurring during 28–29 January 2014. Table 1 summarizes the instruments used for the analysis of the observed ephemeral TMZ, with related locations and operation times. The flow velocity across the lower portion of the water column (a bit more than 1 m from the bed) was collected at both river quadpods and QS2, which were equipped with two velocity profilers (Nortek HR Aquadopp, 2 MHz, sampling at 2 Hz for 45 min/h), the seabed location was recorded by a pencil-beam sonar (Imagenex 881A, sampling at 1 MHz and scanning 10 lines per hour, orientation fixed with the pod, straight line profiling and sonar working as an altimeter) and the surface level was detected by a pressure sensor (sampling at 2 Hz for 45 min/h). The velocity profilers were programmed with a 10-cm blanking distance,

Table 1
Instrumentation deployed during January 2014 experiment and used for the present work (see also Brocchini et al., 2017).

Operation Time	Location		Instrument	#
24–25 January (BS)	−400m	**QR2**	Velocity profilers	2
			Pencil-beam sonar	1
			Pressure sensor	1
	+640m	**QS2**	Velocity profilers	2
			Pencil-beam sonar	1
			Pressure sensor	1
28–29 January (SS)	−400m	**QR2**	Velocity profilers	2
			Pencil-beam sonar	1
			Pressure sensor	1
	−290m	**QR3**	Velocity profilers	2
			Pencil-beam sonar	1
			Pressure sensor	1
24–25 January & 28–29 January (BS, transition, SS)	+900m −10km	**QS3** **RG**	ADCP hydrometer	1 1
	lighthouse near MR mouth	**weather station**	–	1
	Ancona harbor, 25 km South of Senigallia	**tide station**	–	1

with an uplooking profiler with bin size of 5 cm and a down-looking profiler with bin size of 2 cm (40 total bins in the combine profile), while the overlap region between the velocity profilers occurs near 0.4 m above the bed. QS3 was only equipped with an ADCP which enabled the recording of the wave characteristics every hour (see also Brocchini et al., 2017).

Additional observations of environmental conditions during the field experiment were used in the analysis that follows. First, data collected by a weather station located on top of the harbor lighthouse (Fig. 1c) was used to quantify wind speed and direction and precipitation. To better quantify the river forcing and estimate the timing of peak discharge, the river stage was measured every half an hour by the river gauge (RG hereafter) located at the Bettolelle station (Fig. 1b). The RG is located about 10 km upriver of the MR mouth and was the closest to the mouth among all hydrometers existing along the MR during the experiment (see also Melito et al., 2020).

Water and sediment samples were collected from the MR estuary from a small boat during quiescent periods between or immediately following storm events when safe weather conditions were ensured. Water column observations were carried out once per day at several stations (see Fig. 1c) during the period between the two storms on the morning of 26 January 2014, approximately between 11.00 and 14.30 (white circles) and 27 January 2014, approximately between 10.00 and 13.00 (yellow circles). Similar sampling was conducted immediately after the SS on the morning of 29 January 2014, approximately between 10.00 and 13.30 (red circles). Observations spanned more than 1 km along the final 700 m of the MR out to about 500 m offshore of the MR mouth. Vertical profiles of temperature, pH, salinity, and turbidity were logged at select locations at 0.5 m depth intervals using a pre-calibrated Hach Quanta Hydrolab® water quality sonde. Details on sediment type and median grain size are presented in Brocchini et al. (2017).

Water sampling and relevant measurements were used to estimate additional terms useful for a spatio-temporal description of the estuarine stratification during the field experiment. Specifically, water density in the MR estuary was reconstructed on the basis of pressure, temperature and salinity[2] (Gill, 1982), which were obtained from the water samples and cast data. Based on these data and results, a stratification parameter was estimated as:

$$\eta_S = \frac{\Delta S}{S_m} \tag{1}$$

where ΔS is the difference between bottom and surface salinity values, and S_m is the average between bottom and surface salinity. The water column is well-mixed when $\eta_S < 0.1$, partially mixed if $\eta_S = (0.1 - 1)$ and stratified for $\eta_S > 1$ (Prandle, 2009; Restrepo et al., 2018).

2.3. Flocculation model

Since the flocculation is one of the main mechanisms controlling the fate of fine sediments and contaminants in estuaries (Manning et al., 2010), its understanding is strongly related to the TMZ formation. To investigate the potential relative depositional effects leading to the TMZ formation within the MR and due to the lack of floc settling measurements during the field campaign, an existing flocculation model (FM) suite was used (Manning and Dyer, 2007; Spearman and Manning, 2008; Manning et al., 2011). The FM is based on actual floc settling velocity and floc mass distributions (approximately 200 floc populations) from a wide range of turbulence and SSC conditions, and flocs are composed from different sand-mud mixtures. The approach follows the concept of macrofloc (size>160 μm) and microfloc (size<160 μm) (Krone, 1963; Eisma, 1986), whereby the former floc type is constructed from the latter. The input parameters include SSC, sediment type/mixture, and turbulent shear stress, while the outputs include macrofloc settling velocity (Ws_{MACRO}), microfloc settling velocity (Ws_{micro}), ratio of floc mass between the two size fractions (SPM_{ratio}), and the total mass settling flux (MSF), as outlined in Appendix B.1.

The FM was applied to the MR estuary through assessment of three scenarios, i.e. SS, BS and transition between the storm events. Spatially, three points along the MR transect were considered: i) inland (~500m upriver of the mouth); ii) mid-zone (approximately at the mouth); iii) seaward region (~500m offshore of the mouth). Depth-wise focused on two profile points were chosen at each location, 0.25 m above the bed, where flocculation tends to be highly significant (Mehta and Lott, 1987), and a local mid-depth position. To run the FM, suitable input values are needed. To this aim, the SSC range was obtained from a relative comparison from the turbidity measured during the water and sediment samples. High SSC values are in the region of 2500 mg/L and for this scenario comparison assessment, this was deemed equivalent to the peak measured 250 NTUs. Hence, the NTUs at each scenario assessment point were nominally converted to SSC equivalent values using 1 NTU = 10 mg/L (see also the experimental findings at Section 3.3).

The suspended sediment composition at each location was based on both previous MR studies and samples taken during January 2014 (Brocchini et al., 2015, 2017). For the FM, the following nominally representative mud:sand (M:S) compositions were considered: both 100M:0S and 75M:25S at the inland (TMZ) site, 50M:50M equal mud/sand mixture at the mid-zone, and it was assumed to be pure sand (0M:100S) in the seaward region. The level of flocculation primarily depends upon the combined effects of SSC and turbulent mixing. To provide a comprehensive assessment of flocculation, the turbulent shear stresses at each location used by the FM were based on a range typically experienced in many tidal estuarial locations: 0.06, 0.35, 0.6, and 0.9 Pa.

3. Results

During the observational period of the field experiment, two winter storms occurred from 24–25 January 2014 and 28–29 January 2014, respectively. The former storm (BS) was characterized by high energy waves and was mainly driven by NNE winds (Bora), while the latter storm (SS) was driven by less intense winds coming from NNW. River discharge was significantly different during the two events.

3.1. Big (Bora) storm versus small storm

Fig. 3 summarizes observations made during the storms that occurred on 24–25 January 2014 (BS) and 28–29 January 2014 (SS) at QR2. Fig. 3a shows mean precipitation in the watershed and the river stage observed at the Bettolelle station, ~10 km upriver of the mouth. The timing of the peak stage at the Bettolelle station and at the mouth is indicated (vertical light blue lines). The time for the peak stage to travel from Bettolelle station to the station of Ponte Garibaldi (~1.5 km upriver of the mouth and operating since 2016) was ~1.25 h during flood events recorded in 2018 (Melito et al., 2020). Consequently, for this work, the time for the peak stage to travel from Bettolelle station to the mouth was estimated ~1.5 h as well.

Fig. 3b shows the water surface levels observed at the nearby Ancona harbor (black lines), which provides surge and tidal data applicable to the Senigallia area with negligible delay (Brocchini et al., 2017). The instantaneous water levels observed at QR2 (red lines) and QR3 (yellow line) are also shown. The wave conditions are illustrated in Fig. 3c showing significant height H_s (circles), peak period T_p (black lines) and peak direction (colors of circles, see color bar). Fig. 3d illustrates both mean speed (refer to vertical axes) and direction (refer to color bars) observed by the Aquadopps at QR2 (circles) and QR3 (diamonds). The

[2] Gabriel Ruiz-Martinez (2022). Seawater density from salinity, temperature and pressure (https://www.mathworks.com/matlabcentral/fileexchange/85900-seawater-density-from-salinity-temperature-and-pressure), MATLAB Central File Exchange. Retrieved January 31, 2022.

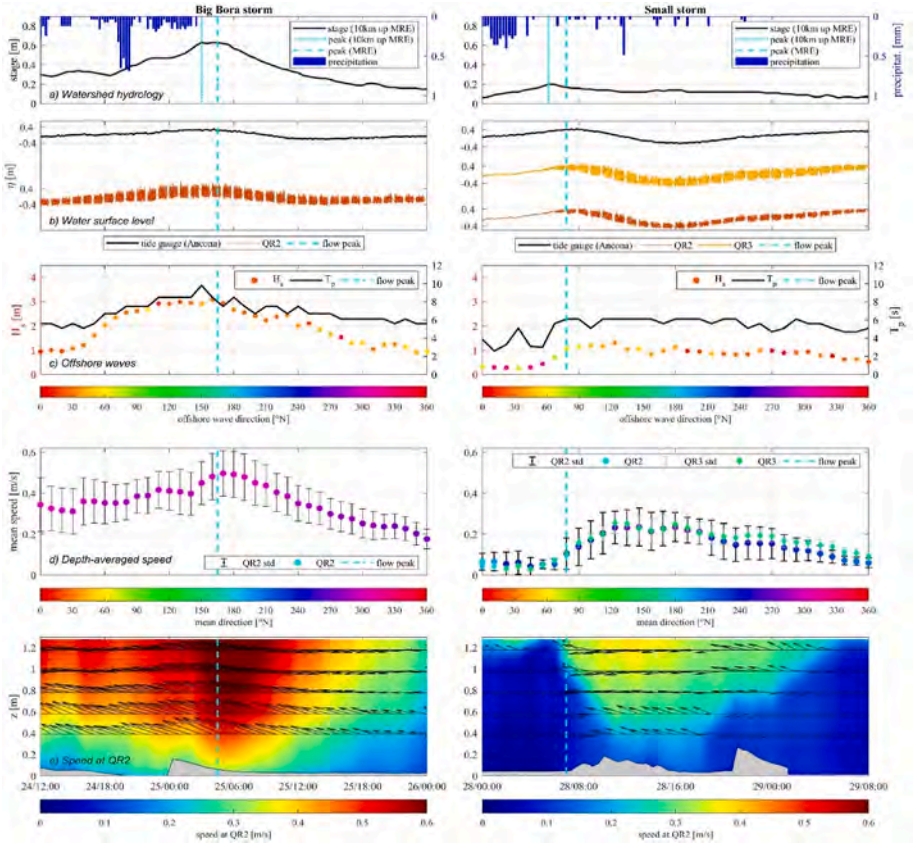

Fig. 3. Observed environmental conditions for BS (left panels) and SS (right panels). a) Mean precipitation in the watershed (blue bars) and stage at Bettolelle (~10 km from the MR mouth, black line). b) Water surface level recorded by tide gauge (Ancona, black line) and sensors at estuary (QR2, orange line; QR3, yellow line). c) Significant wave height and incoming direction (colored dots), and peak period (black line) at QS3. d) depth-averaged speed with mean direction (colored symbols) and standard deviation (error bars) at QR2 and QR3. e) Vertical distribution of speed, with direction shown by arrows at QR2 (upward indicates north), and bed estimates (w.r.t. quadpod deployment) from pencil beam sonar (grey areas). In each panel, light blue vertical lines indicate the timing of the flow peak at Bettolelle (solid) and MR mouth (dashed). (For interpretation of the references to color in this figure legend, the reader is referred to the Web version of this article.)

values are depth-averaged along the considered depth and are represented together with their standard deviation (black error bars for QR2, grey for QR3), which describes the (more or less pronounced) vertical variation of the horizontal speed.

Fig. 3e illustrates the hourly-averaged speed along the water column observed at QR2. The speed directions (upward indicates north, i.e. 0°) at four horizontal layers are also shown using black arrows. However, such speeds are not perfectly downriver (the river orientation at QR2 suggests a direction slightly larger than 0°N, as shown in Fig. 1d), because the collected data only refer to the lower water column (the total water depth being ~2.5m at QR2, see Fig. 1e) and because of the generation of secondary/cross-river flows, consequence of the nearby bend (~100 m downriver of QR2). In addition, the momentum induced by the incoming sea waves contributes differently to the flow directionality during the recorded time, as it can be observed during the BS or at the SS wave-height peak (high- or moderate-flow conditions) and before or after the SS wave-height peak (low-flow conditions). Although measurements in the upper water column were not collected during the whole experiment, a clear upriver flow (direction in the range 180–240°N) was recorded in the lower water column at QR2 during the tail of the SS (latest stages plotted in Fig. 3d) and quiescent conditions (see section 3.4), this suggesting a region with large shear in the mid water column, which connects an upriver flow (lower column) with a downriver flow (upper column).

To better quantify the turbidity during the two events, the backscatter amplitude is illustrated in Fig. 4. While it is possible to estimate the magnitude of suspended particulate using the backscatter amplitude, a separate, direct measure of sediment concentration is needed to calibrate the backscatter across the profile. Lacking the additional measurements needed to perform a calibration, we have applied a demeaning approach to each bin of each beam separately, to remove beam pattern and environmental biases, as successfully applied to multibeam echosounder data (de Moustier and Kraft, 2013). Such result more accurately represents the relative magnitudes (i.e., gradients) of SSC across the profile, which are more consistent with the sonar saturation observed at QR3 (see section 3.2).

Observations at QR2 during BS show that high seaward river discharge through the estuary (stage ~0.6 m at Bettolelle) competed

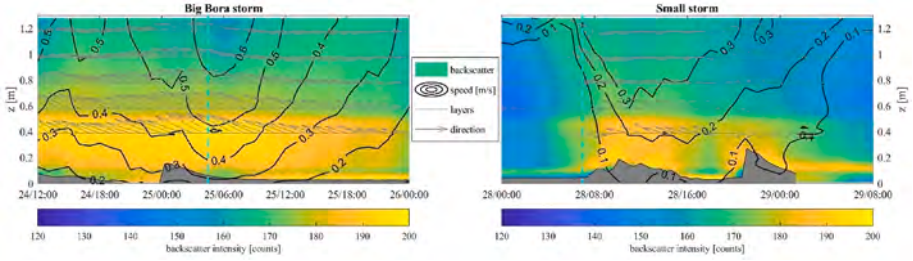

Fig. 4. Observations during BS (left panels) and SS (right panels) were made at QR2 for the acoustic backscatter intensity along the water column (color maps), speed (contour lines) and velocity directions (arrows). The location of the riverbed estimated from hourly averages of the pencil beam sonar line scans is overlaid in grey. (For interpretation of the references to color in this figure legend, the reader is referred to the Web version of this article.)

with significant landward forcing from the sea (wave height >3 m at QS3 and >0.5 m at QR2 recorded during high tide) at the estuary (Fig. 3a–c, and Melito et al., 2020). As a result, the longitudinal flow direction along the water column was downriver but there was also some secondary circulation, with a depth-averaged speed ~0.5 m/s during the peak (Fig. 3d and e). The high backscatter observed during the whole BS event suggests large sediment re-suspension, especially in the lower water column (Fig. 4, left panel).

The SS resulted in different hydrodynamic conditions in the MR estuary, with moderate river discharge (stage ~0.2 m at Bettolelle) and milder wave action (wave height ~1 m at QS3 and <0.1 m at QR2) during the peak (Fig. 3a–c), with the wave forcing increasing at the MR mouth after the peak (~0.3 m at QR2). Hence, depth-averaged speeds were relatively low and the maximum value (~0.25 m/s) occurred 4 h after the peak, suggesting that: 1) river flow was mostly localized within the upper water column (z > 1.3 m, not captured by the observations); 2) an important river-sea interaction occurred (Fig. 3e), as also testified both by the modification of the flow directionality (black arrows) and by the ratio between standard deviation and depth-averaged speed (~0.45, Fig. 3d). Varying directions characterize the water column and strongly change with time, with inflowing at lower layers and outflowing at the upper layers during the flow peak/high tide and during the following flood tide (around 20:00 of 28 January), vice versa during the low tide (around 16:00). Further, a persistent salt wedge intruded onto the river in the lower water column with a buoyant river plume in the upper water column at QR3, where the vertical shear was less evident than upriver (Fig. 3d). The high backscatter at QR2 (Fig. 4, right panel) testifies that a high turbidity remains within the lower water column (z < 0.7 m) for about 16 h (from 28/01 at 8:00 to 29/01 at 00:00), i.e. the time during which the offshore wave height oscillates around 1 m.

The comparison between BS and SS in terms of energy and energy flux in the offshore region (i.e., at QS3) is illustrated by the following equations:

$$\left(\frac{H_{s,BS}}{H_{s,SS}}\right)^2 \sim \left(\frac{3}{1}\right)^2 = 9 \tag{2}$$

$$\left[\left(\frac{H_{s,BS}}{H_{s,SS}}\right)^2 \frac{c_{g,BS}}{c_{g,SS}}\right] \sim \left[\left(\frac{3}{1}\right)^2 \left(\frac{6.8}{3.9}\right)\right] = 16 \tag{3}$$

where H_s and c_g represent, respectively, the significant wave height and group speed estimated offshore during BS and SS. Eq. (2) is the ratio between the wave energy estimated during BS and the wave energy during SS, showing that the offshore energy is 9 times larger during the BS than during the SS. Similarly, eq. (3) gives the ratio in terms of energy flux, revealing that such quantity is 16 times larger during BS. Moreover, a strong energy decay occurred at the estuary during the BS peak, although only a slight dissipation characterized the wave propagation from QS3 to QS2. Specifically, the total significant height drops to $H_{s,BS} \sim 0.5m$ at QR2 (about 17% of that recorded at QS3), mainly due to the strong breaking close to the mouth that provided a large drop of the sea-swell component, while the lower-frequency/infragravity waves were almost unaffected and propagated upriver almost unaltered (Melito et al., 2020). Much smaller is the dissipation during the SS, when the total significant height drops to $H_{s,SS} \sim 0.3m$ at QR2 (about 30% of that recorded at QS3). Hence, although the reduced wave energy coming from the offshore during the SS, a smaller breaking at the mouth promoted the wave penetration within the MR, which is also facilitated by the less intense river flow. Such occurrences contributed to: i) a pronounced interaction between river and sea, ii) a high turbidity and stratification within the final reach of the MR (see also implications in terms of floc dynamics at Section 3.4), iii) the generation of a convergence zone between QR2 and QR3.

3.2. Characterization of the small storm

During the SS, observations in the lower reach of the MR suggest the persistence of a density gradient that was modulated in space (between QR2 and QR3) and time by the local surge, as testified by the signature of a buoyant river plume, evident in the uppermost recorded region. Specifically, before the flow peak (light blue vertical line), at QR2 there was a stronger, more coherent downriver current in the upper water column (z > (1–1.2) m, purple region in Fig. 5b$_1$), a thin layer of cross-river flow, bending leftward, just below (z > (0.8–1) m, blue region) and a weak upriver (sea intrusion) current (<0.1 m/s) in the lower water column (z < (0.8–1) m, green region). Conversely, before the flow peak at QR3, the current was nearly stagnant (<0.1 m/s) with mean direction nominally upriver across the vertical (green region in Fig. 5b$_2$), but characterized by oscillations and larger variance, with occurrence of some cross-river/secondary flows in the range (55–140)°N (yellow regions). A clearer view of the longitudinal velocity components is provided in Fig. 5c$_1$, c$_2$, where rightward/leftward arrows represent the downriver/upriver flows. At both locations, the backscatter exhibited a vertical gradient with a maximum at the bed (e.g., see Fig. 4b for what concerns QR2, not shown for QR3). Here, the maximum backscatter value at QR2 (~170) was a bit smaller than the value at QR3 (~200).

After the peak stage (shaded area), the horizontal velocity followed the tide evolution, with the flow direction in the lower part changing from mainly upriver (green) to mainly cross-river (blue) at QR2, and the cross-river flow extending to the bed during the low tide (Fig. 5b$_1$). Looking at the longitudinal components, the ebb tide and part of the flood tide are dominated by an interplay between river forcing and sea waves (orange and purple profiles in Fig. 5c$_1$), which modified the classical seawater-intrusion pattern observed before and after the storm (see also Appendix A.1), and significantly affected the riverbed evolution, as testified by the sonar recordings (grey region). A near-bed stratification is highlighted by the backscatter signal during the ebb and following flood tide (Fig. 4b, yellow tones).

The sea action was predominant at QR3, with the tide modulating the generation of cross-river/secondary flows (Fig. 5b$_2$), observed all along the lower water column. Further, downriver flows were almost negligible, while the sea waves played a major role and forced the flow to propagate upriver (Fig. 5c$_2$). In agreement with the backscatter increase, the pencil beam sonar detected the onset of sediment deposition at 06:00 on 28 January (just prior to the peak flow), then the bed level kept growing until the blanking distance of the pencil beam was exceeded (around 10:00) and started to decrease when the SS began to subside (morning of 29 January). Sediment deposition was evident during the mechanical recovery of QR3 (Brocchini et al., 2017), and is demonstrated by the water elevations observed at QR2 and QR3 (Appendix A.2).

3.3. Water and sediment samples

During the post-storm to quiescent period between the two storms (on 26 and 27 January) and after the SS (on 29 January), *in situ* sampling operations occurred (see Section 2.2). The timing of sampling conducted during the mornings of 26 and 27 January are shown by the shaded areas in Fig. 6 to provide context with the overall hydrodynamics. Each sampling period had similar wind speeds (Fig. 6a). The first sampling period (26 January) occurred during low tide, with larger wave heights both nearshore (0.3 m–0.4 m, Fig. 6d) and within the estuary (Fig. 6b), and larger speeds at QR2 (Fig. 6c). The second time period (27 January) occurred during ebb tide, with smaller wave heights (0.1 m–0.15 m) and smaller mean speeds and standard deviations at QR2. As before (Fig. 5b$_1$), the tide influence was relevant at QR2 (Fig. 6e$_1$, f$_1$), while the speed close to the bed at QS2 was relatively small during the sampling period (Fig. 6f$_2$), with directions rapidly changing (Fig. 6e$_2$), in agreement with the wave direction (Fig. 6d).

Riverbed samples were also collected in the final reach of the MR

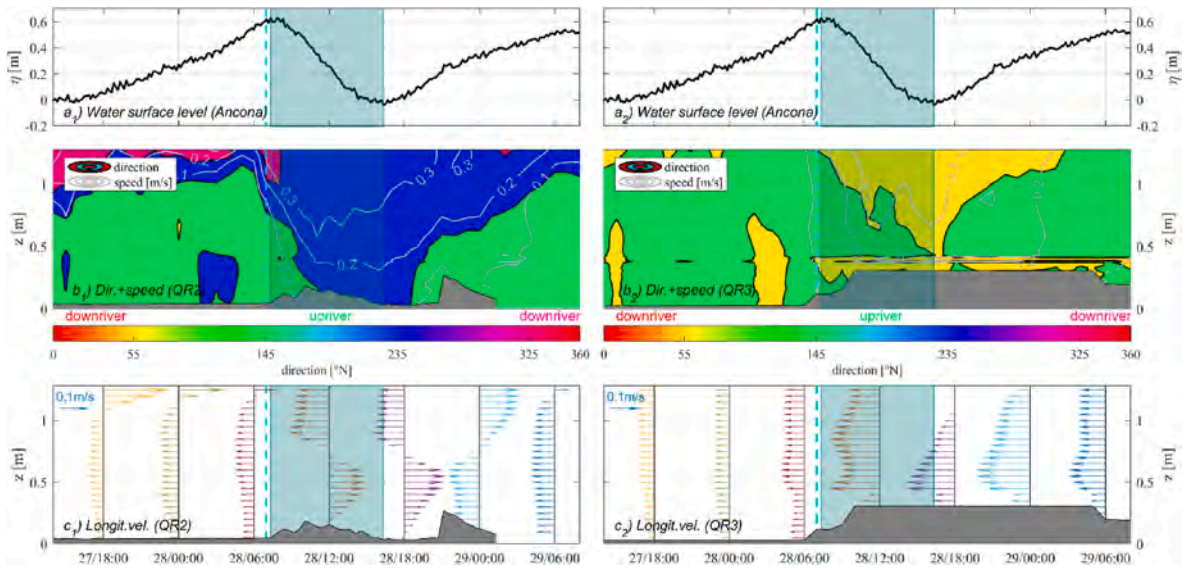

Fig. 5. Data collected during the SS. a) Water surface level measured by the tide gauge (Ancona). b) Speed (contour lines) and velocity directions (color map) at QR2 and QR3. c) Longitudinal velocity component (between 27/01/2014 at 18:00 and 29/01/2014 at 06:00, every 6 h). The location of the bed estimated from hourly averages of the pencil beam sonar line scans is overlaid in grey. Shaded areas highlight the period during which ebb tide occurred. (For interpretation of the references to color in this figure legend, the reader is referred to the Web version of this article.)

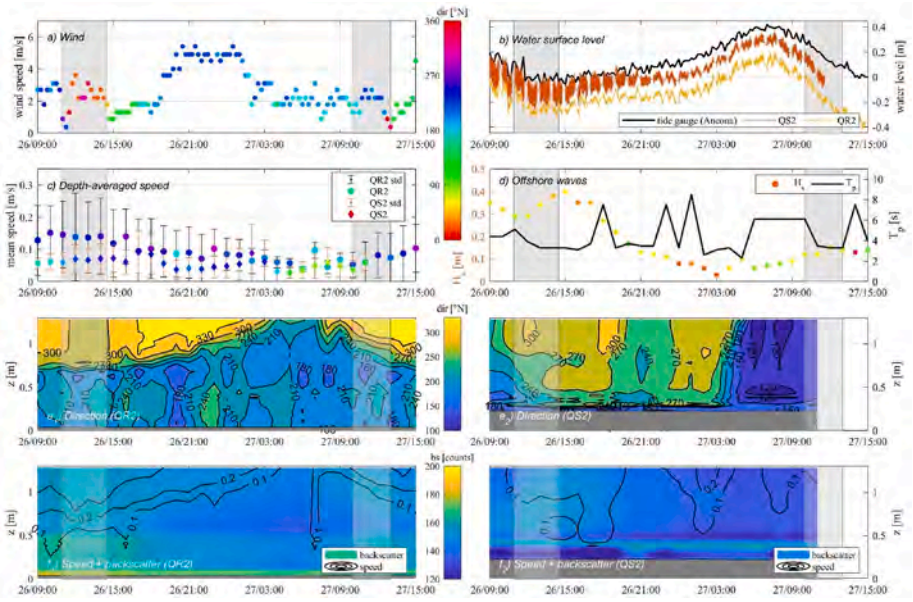

Fig. 6. Data collected during the quiescent period. a) Wind at the estuary. b) Water-surface level recorded by tide gauge (Ancona) and sensors at MR estuary (QR2, QS2). c) Depth-averaged speed with mean direction (colored symbols) and standard deviation (error bars) at QR2 and QS2. d) Offshore wave characteristics (QS3). e) Velocity directions at QR2 and QS2. f) Speed (contour lines) and backscatter intensity (color map) at QR2 and QS2. Shaded rectangles give the time during sample collection. (For interpretation of the references to color in this figure legend, the reader is referred to the Web version of this article.)

during the quiescent periods prior to the BS, between BS and SS, and after the SS. Large concentrations of gravel were observed in the central portion of the river, which also contained accumulations of terrigenous organic matter (detrital vegetation) during the whole experiment (e.g., before the BS storm at QR1 and after the SS at QR3). The fine-grained sediment within the entire final reach was characterized by fine silt, clay and siliceous minerals, with dominance of montmorillonite. Moving downriver, fine sand was observed starting from the mouth up to the offshore quadpods. The fine sand also dominated re-suspended sediments, which were found in water samples collected between the final reach of the MR and ~1.3 km offshore, i.e. at the plume edge. Flocculated particles were also found in the water column, with the sizes of the natant flocs larger on 26 January than on 27 and 29 January, suggesting floc aggregation into larger flocs when the BS/SS subsided, followed by subsequent deposition (Brocchini et al., 2017).

In the beginning of the quiescent period, i.e. during the tail of the BS (26 January), the 3.5–5 m deep seaward region was generally well-mixed (salinity 22–24 ppt, Fig. 7a, temperature 8.5–9 °C, Fig. 7b), with just the surface 0.5 m displaying colder, fresher water. Turbidity was less than 50 NTU, with water sample analysis indicating primarily fine sandy sediments present. About 300 m upriver from the mouth, the depth had shallowed to 2 m, and the likely sediment re-suspension caused by the higher river flow induced during the BS led to a more than doubling (~130 NTU) of turbidity (Fig. 7c) as compared to observations in the seaward region. The re-suspended muddier sediments present at −0.3 to −0.6 km zone would exhibit much stronger flocculation kinetics than the less cohesive (higher sand content) suspension in the MR approaches. The inland water was cooler (7 °C), less brackish (salinity <2 ppt in the surface 1 m), and a sharp halocline developed within the 1–1.5 m-deep region.

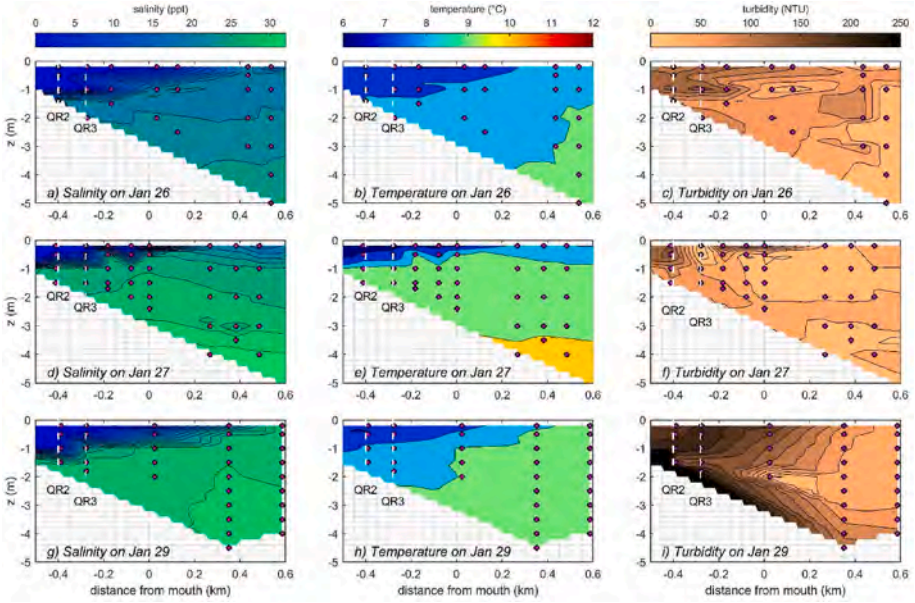

Fig. 7. Data from samples (indicated by dots) collected at the estuary on 26 January (top row), 27 January (middle row) and 29 January (bottom row): a-d-g) salinity; b-e-h) temperature; c-f-i) turbidity.

The transitional period between the passing of the BS and the run-up to the SS (27 January), resulted in warmer (~1 °C) and more saline (>28 ppt) well-mixed water column conditions within the MR system (Fig. 7d and e). There was some partial stratification with cooler (<8 °C), less saline (<10 ppt) conditions in the (0.5–1) m surface water inland from the mouth of the MR. Turbidity levels (Fig. 7f) were generally halved from those observed during the tail of the BS, ranging from 25 to 80 NTUs for the seaward and inland regions, respectively. This would equate to a significant reduction in particle interactions for flocculation, especially in the MR inner region (between −0.3 and −0.6 km), where the higher turbidity levels in the upper water column suggests a riverine origin for the suspended sediments.

The transitional period after the SS during the morning of 29 January promoted partial mixing in the upper part of the water column through the MR leading to a higher degree of stratification. This is demonstrated by the steep haloclines formed post SS as indicated salinities spanning 0–26 ppt in the upper 1 m of the water column (Fig. 7g). Warmer (~9 °C) (Fig. 7h) seawater encroached 400 m further inland during the SS than during the BS. A notable feature is the formation of a TMZ (Fig. 7i) in the inner MR channel post-SS in a region where the sediments are seen to be predominantly cohesive (Brocchini et al., 2017). Fig. 7i shows a turbidity gradient progressively building seaward to landward, with maximum turbidity levels exceeding 180 NTU. Observed turbidity levels approaching 250 NTU (0.3–0.5) m above the bed in the < −0.3 km region suggests the formation of a concentrated benthic suspension (CBS) layer (Wolanski et al., 1988; Ross and Mehta, 1989); these types of features have been observed in many traditional estuarine TMZs. CBS layers have the potential to set-up turbulence damping and drag reduction effects (Best and Leeder, 1993; Li & Gust, 2000; Dyer et al., 2004; Manning et al., 2006), and importantly, this environment would be highly conducive for stimulating flocculation (Manning and Bass, 2006; Gratiot and Manning, 2008).

3.4. Indicative floc dynamics

As described in Section 2.3, a FM was initialized using the turbidity measurements illustrated in Fig. 7, as well as on the analysis described in previous studies (Brocchini et al., 2015, 2017). To examine the resultant formation of the TMZ and flocculation at each location for a nominal period of time (as opposed to a continual timeline of stratification generation), the FM output computed at moderate shear stress level of 0.35 Pa was used as a benchmark turbulence level, in order to facilitate the various scenario intercomparisons and in agreement both with previous flocculation TMZ studies (e.g., Manning et al., 2017) and with the stress levels estimated at QR2. Specifically, the shear stress values have been evaluates as

$$\tau = \rho \nu_t \frac{dV}{dz} \tag{4}$$

where V is the horizontal velocity, $\rho = 1000 kg/m^3$ is the water density (here assumed as constant), while the eddy viscosity is defined as

$$\nu_t = \kappa u_* z \left(1 - \frac{z}{d}\right) \tag{5}$$

with $\kappa = 0.41$ being the von Karman's constant and d the instantaneous water depth. The shear velocity is defined using the logarithmic velocity distribution (e.g., Bagherimiyab and Lemmin, 2013):

$$\frac{V}{u_*} = \frac{1}{\kappa} \ln\left(\frac{z}{z_0}\right) \tag{6}$$

where the bed roughness is estimated as $z_0 = d_{50}/30$ and the median grain diameter in the final reach of the MR is taken as $d_{50} \sim 62.5 \mu m$, corresponding to the separation between very fine sand and silt (e.g., Brocchini et al., 2017; Baldoni et al., 2021). The result is illustrated in Fig. 8b, where the whole water column is characterized by relatively small values, never exceeding 0.9 Pa during the sampling activity (shaded grey areas).

The FM outputs for the three scenarios at each location are shown in Table 2, Table 3 and Table 4, while the complete FM outputs and run parameters related to 0.25 m above the bed (at all shear stress levels) are summarized in Appendix B.2.

The link between the FM findings and the TMZ structure mainly concerns the transport of fines and contaminants, as well as the floc settling and depositional effects affecting the TMZ. Such aspects are discussed in Section 4.

4. Discussion

Net estuarine circulation in MTEs similar to the MR estuary is

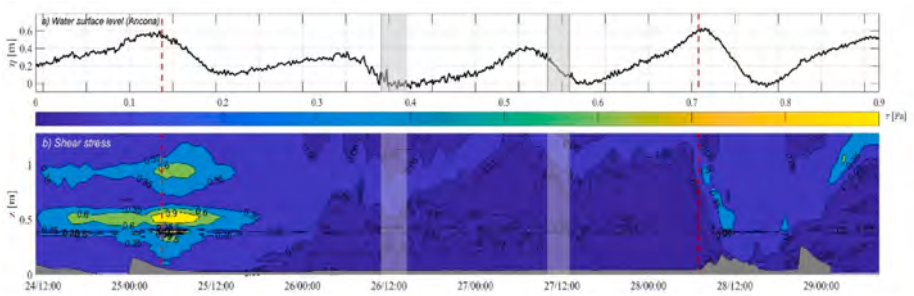

Fig. 8. Data referring to the BS, transition and SS periods. (a) Water surface level measured by the tide gauge (Ancona). (b) Computed shear stress. The bed estimated from the pencil beam sonar line scans is overlaid in grey. Shaded rectangles give the time during sample collection, while the red vertical lines indicate the timing of the flow peak at the MR mouth. (For interpretation of the references to color in this figure legend, the reader is referred to the Web version of this article.)

Table 2
FM outputs for scenario 1 (SS): floc characteristics 0.25 m above bed.

Distance from mouth [km]	Mud [%]	Sand [%]	Turbidity [NTU]	SSC [mg/l]	Ws_{macro} (0.35Pa) [mm/s]	Ws_{micro} (0.35Pa) [mm/s]	SPM_{ratio}	MSF (0.35Pa) [mg. $m^{-2}s^{-1}$]
−0.475	100	0	250	2500	3.49	0.93	7.89	8010
−0.475	75	25	250	2500	4.15	0.97	2.16	7849
+0.025	50	50	155	1550	2.79	2.24	0.84	3854
+0.525	0	100	65	650	6.80	6.80	1.00	4420

Table 3
FM outputs for scenario 2 (BS): floc characteristics 0.25 m above bed.

Distance from mouth [km]	Mud [%]	Sand [%]	Turbidity [NTU]	SSC [mg/l]	Ws_{macro} (0.35Pa) [mm/s]	Ws_{micro} (0.35Pa) [mm/s]	SPM_{ratio}	MSF (0.35Pa) [mg. $m^{-2}s^{-1}$]
−0.475	100	0	130	1300	2.93	0.93	4.71	3351
−0.475	75	25	130	1300	3.19	0.69	1.41	2795
+0.025	50	50	80	800	2.39	2.10	0.62	1768
+0.525	0	100	40	400	6.80	6.80	1.00	2720

Table 4
FM outputs for scenario 3 (transition): floc characteristics 0.25 m above bed.

Distance from mouth [km]	Mud [%]	Sand [%]	Turbidity [NTU]	SSC [mg/l]	Ws_{macro} (0.35Pa) [mm/s]	Ws_{micro} (0.35Pa) [mm/s]	SPM_{ratio}	MSF (0.35Pa) [mg. $m^{-2}s^{-1}$]
−0.475	100	0	100	1000	2.79	0.93	3.86	2403
−0.475	75	25	100	1000	2.95	0.61	1.19	1884
+0.025	50	50	65	650	2.31	2.07	0.58	1403
+0.525	0	100	25	250	6.80	6.80	1.00	1700

typically determined by an important interplay between the freshwater discharge and sea forcing. Even with low tide ranges and negligible tidal currents, tidal forcing does influence the MR estuary under all freshwater conditions, especially in the lower reach, through a low-frequency modulation of river current and sea waves. About 300 m upriver of the mouth, the sea action (wind, wave, tides) is generally larger than the freshwater forcing (river discharge), thus promoting an overall net landward flow of water from coastal sources in the lower water column during quiescent periods and small storms. Similarly, ~400 m upriver from the mouth, there is a net landward flow of seawater in the lower portion of the water column during quiescent periods, whereas freshwater flows gravitationally seaward in the upper portion of the water column. The higher tide level, the thicker the seawater-intrusion layer.

Small storms like those observed in this study, however, lead to an interesting interplay between sea waves and river forcing. Severe storms result in freshwater discharge overwhelming seaward forcing upriver of the mouth resulting in a homogeneous freshwater column characterized by downriver seaward flow and negligible tidal modulation. In the context of TMZ formation at the MR estuary, three different scenarios are considered: 1) the episodic moderate-flow regime (represented by the SS), consisting of alternating landward-seaward flows and cross-river flows; 2) the episodic high-flow regime (represented by the BS), consisting of seaward flow across the entire observed water column; 3) the base low-flow regime (represented by the transitional, quiescent period between the BS and SS).

During scenario 1, both river discharge and waves at the MTE mouth are important. Specifically, during the whole SS, both river flow and onshore wave energy remained nearly constant at the boundaries, i.e. at Bettolelle station and offshore (QS3). However, the lower river flow (during the ebb tide, at low tide and in the beginning of the flood tide) facilitated the propagation of low-energy/non-breaking waves into the estuary, thus leading to a strong interaction between river forcing and waves at the mouth, which affected both gravitational circulation and TMZ generation. In other words, the storm-induced conditions (moderate river flow and increased onshore wave energy) strongly modified hydrodynamic conditions in the lower reach of the MR during the SS, transitioning from a net landward-seaward flow (i.e. salt-wedge behavior during lower-flow conditions) to a mainly cross-river flow (more moderate-flow conditions). During this circulation regime, neither the river discharge nor onshore wave energy prevailed, and significant sediment re-suspension occurred as a consequence both of the river- and wave-driven fast flows and of the high shear stress that

generated within the recorded water column (Fig. 8b). High-turbidity regions were thus generated between the two recorded sections, with material being eroded and/or re-suspended at QR2 and transported downriver until flow energy started to reduce in relation to onshore forcing, contributing to a large sediment deposition at QR3 during the ebb tide. These factors led to an ephemeral TMZ localized between QR2 and QR3, this being also supported by the strong shear stress observed at QR2, which provided an increased sediment transport, partially compensating the weak tidal mixing typical of MTEs and the existing moderate flow condition.

Just after the SS, the turbidity values in the lower estuary were significantly larger than those offshore. These results can be coupled with the significant salinity gradient and the well-stratified structure at a distance of 300–600 m from the mouth, as suggested by the water density (Fig. 9c), which reveal a density gradient from the surface (~1000 kg/m^3) to the riverbed (~1023 kg/m^3). Stratification significantly varied along the longitudinal transect, as shown by the longitudinal distribution of η_S (yellow line, Fig. 9d). The upriver/inland region was characterized by a high degree of stratification level ($\eta_S > 1$), while the mid-zone region, just off the MR mouth, was partially mixed ($\eta_S < 1$). Stratification further decreased from the mid-zone moving toward the mouth of the MR estuary and into the offshore region ($\eta_S < 0.1$), where well-mixed conditions existed. Furthermore, significant flocculation and fast macrofloc settling occurred where the TMZ generates. The bio-cohesion from pure mud would have greater cohesive effects and improve interparticle collision efficiency, also considering a larger macrofloc growth due to the highly cohesive montmorillonite mineral (Brocchini et al., 2015). A less cohesive sediment composition would provide a faster floc settling and a less efficient flocculation. The less turbid and less stratified zones downriver of the TMZ were characterized by slower macroflocs and quicker microflocs (lower river) or by much quicker flocs (sea), as well as much smaller MSF peaks compared to those within the TMZ, but still greater than the assumption of a constant 0.5 mm/s. All the above results suggest that the observed TMZ during and just after the SS event was a region of high flocculation and significant deposition.

Looking at scenario 1 in terms of a conceptual model (Fig. 10a), the alternation of landward-seaward flows (typical of a low-flow regime) and cross-river flows leads to high turbidity near the bed at the leading edge of the seawater tongue (see the separation between green and blue shades). Cross-river flows are enhanced by the opposing river-sea forcing leading to high shear stress along the water column and resuspension of newly deposited or imported material from the lower estuary. Water column stratification and high near-bed turbidity suggest intense flocculation and large mass settling fluxes, with generation of an ephemeral TMZ downriver (seaward) of the seawater-intrusion tip (see downward arrow).

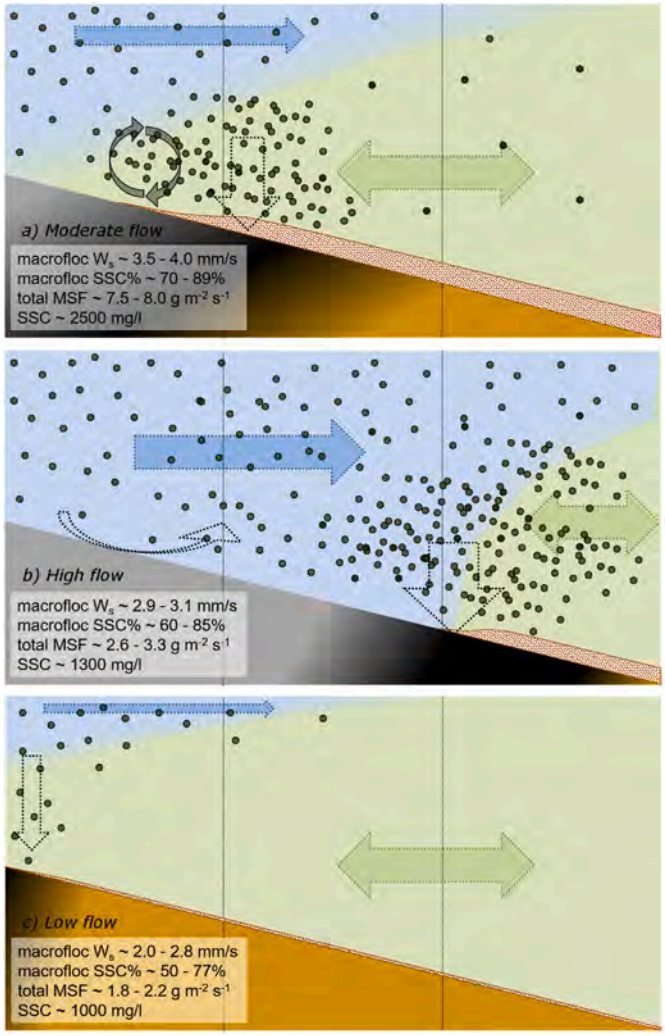

Fig. 10. Conceptual model representing: a) moderate-flow conditions (SS); b) high-flow conditions (BS); c) low-flow conditions (transition). Blue shades and arrows identify the river forcing. Green shades and arrows identify sea forcing (waves and tides). Black and grey arrows show the sediment-particle motion. The vertical thin lines qualitatively indicate QR2 and QR3 locations. (For interpretation of the references to color in this figure legend, the reader is referred to the Web version of this article.)

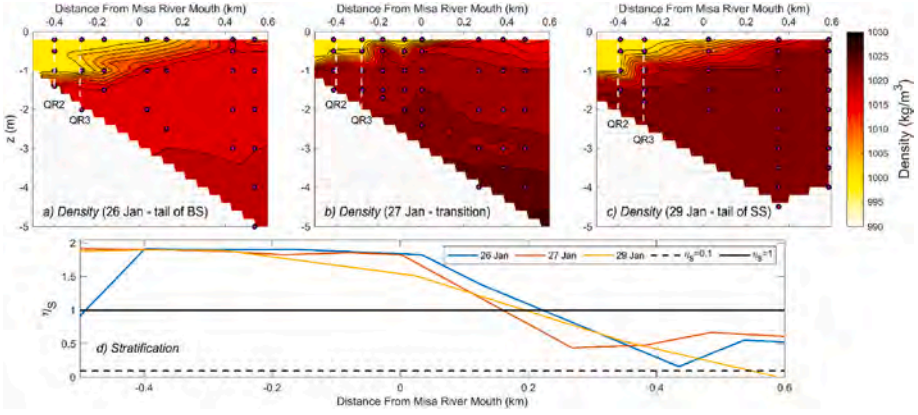

Fig. 9. Estimated density on: a) 26 January, b) 27 January and c) 29 January (sample locations are indicated by dots). d) Stratification parameter during the three sampling days.

During scenario 2, estuarine circulation in the MR estuary was dominated by river discharge, with absence of the seawater-intrusion pattern and expulsion of sediments to sea. The river-discharge predominance also led to a significantly high shear stress before, during and after the storm at QR2 (Fig. 8b), which was induced by the intense flow, providing a high eddy viscosity and shear velocity (see equations (4) and (5)). On the other hand, the sea action was perceived far from the riverbed (e.g., at $z > 0.8$ m), where the higher intensity of the sea-induced momentum modified the directionality of the flow during the peak stage. During the end of BS, the seaward region was characterized by salinity and temperature values similar to those measured during the tail of the SS, although a different stratification regime was observed through the MR estuary (Fig. 9d). Compared to what observed after the SS event, the upriver region was characterized by smaller turbidity gradients and a weaker stratification (Fig. 9d). Further, the SSC at 25 cm above the bed during the tail of the BS was half of that found during the tail of the SS. Specifically, modelled floc settling dynamics were (15–20) % slower and less macrofloc mass was present. Results suggest an increase of turbulence and mixing during the BS, which led to a reduced flocculation, a slower settling and a greater particle dispersion within the water column which, in turn, promoted TMZ suppression near the riverbed (only a thin layer presents some stratification upriver of QR2, as shown in Fig. 9a) during and after the BS event.

In a conceptual model view (Fig. 10b), high-flow conditions lead to a dominance of the freshwater discharge as opposed to seaward forcing (waves and tides), resulting in well-mixed water column conditions in both river and estuary. Such conditions represent "blowout events" with mass export of suspended matter and re-suspended sediment, as testified by visual observation of mats of terrestrial vegetation (Brocchini et al., 2017). The relatively low stratification leads to smaller flocs and much slower settling both around mouth and offshore (see downward arrow).

During scenario 3, the turbidity was significantly low in the seaward area, with the other conditions similar to those observed during the tail of the BS. However, estimated water column density reached values much larger (~1026 kg/m^3) than those observed during the tail of both BS and SS (Fig. 9b), leading to a higher degree of stratification near the MR mouth (Fig. 9d). In the upriver region, the water column was still significantly stratified, with stratification parameters similar to those observed just after the SS (Fig. 9d), as also testified by the variability of the shear stress along the water column, mainly induced by the vertical shear of the velocity (Fig. 8b). A (20–25) % slowing in the floc settling velocities was observed during the transition compared to what found during BS and the settling flux was typically one quarter that observed during SS, with SSC being only (30–40) % of that found during SS. Typically $SPM_{ratio} < 1$, which was indicative of the favoring of smaller microfloc fraction dynamics.

Conceptually, low-flow conditions lead to relatively high turbidity values associated with the freshwater tongue of the MR in the upper water column and sea intrusion in the lower part, with upriver-downriver flow separation continually modulated by the tide (Fig. 10c). A combination of salinity-induced flocculation and bio-cohesion potentially occurs in the final reach, causing settling of fines close to the mouth and increasing their residence times within the estuary.

4.1. Comparison with existing field studies

Looking at the estuarine environments that are typically investigated worldwide, the TMZ in MTEs is mainly induced by gravitational circulation and turbulence damping (e.g., Restrepo et al., 2018), as supposed for the present environment. Specifically, low-flow and episodic high-flow regimes in the MR promote a weakly-stratified environment, as is the case in many temperate estuaries (e.g., Chesapeake Bay, Delware Bay) characterized by moderate-to-strong tidal forcing and weak-to-moderate river discharge. Conversely, episodic moderate-flow regimes in the MR promote strongly stratified to salt-wedge conditions, similar to what occurs in the Columbia River (e.g., Valle-Levinson, 2010). Similar behaviors have been observed in the MTE of the Neretva River (eastern Adriatic Sea), characterized by tide oscillations comparable to those experienced by the MR. Specifically, Krvavica et al. (2016) observed that high flow conditions weaken the stratification, in contrast to typical salt-wedge estuaries, where higher river flows strengthen the stratification.

In addition, based on a long-lasting numerical modeling, Krvavica et al. (2021) state that the river inflow plays the most important role in the salt-wedge dynamics at the Neretva MTE, with sea levels and tides contributing a minor effect. Although the different time scales, such statement seems in contrast with what observed at the MR estuary, where the sea action is fundamental for the overall estuarine dynamics during moderate-flow regimes. In particular, sea waves provide significant mixing beyond tide and river flow in the lower reach of the MR, thus enhancing the gravitational circulation and promoting ephemeral TMZ generation. Under these conditions, as compared to higher flow conditions when the TMZ is typically located landward of the seawater-intrusion tip, it generates seaward (downriver) of the seawater-intrusion tip in the MR estuary. Additionally, the observed stratification is large enough to provide a significant flocculation and large settling, as well as to completely suppress turbulence.

5. Conclusions

During storm conditions, TMZ generation was observed in the MTE of the MR. The TMZ was ephemeral and was only observed during storm conditions when sea waves were impinging on the mouth and the wave impact against the seaward river flow was inducing significant sediment resuspension. No TMZ was present during quiescent conditions in the estuary and adjacent Adriatic Sea. Consequently, differently from meso-to-hyper-tidal estuaries, the tide was not a primary driver of the TMZ generation, but rather serves to modulate the overall water level which in turn can affect location, intensity, and extent of ephemeral TMZs. Observations made during and just after two different storms with different energy levels, show the interplay between river discharge and onshore wave energy in TMZ evolution, and subsequent sediment and suspended load transport in the lower reach of the MR.

A TMZ was present during both storms, although the vertical flow structure and its time evolution were distinctly different. Specifically, the smaller storm (moderate-flow regime) was associated with an interplay between river discharge and sea waves in the lower reach of the river, high turbidity near the bed and significant stratification of the water column. This led to intense flocculation within the estuary, fast mass settling and potential sediment transport towards the mouth. On the other hand, the much greater river current observed during the bigger storm (high-flow regime) produced stronger mixing, reduced the stratification, and pushed the convergence area towards the mouth. Such behavior suggests that the bigger storm either pushed a mixed freshwater pulse out of the mouth of the MTE (the TMZ not showing up) or suppressed the TMZ near the bed by dispersing more of the suspended particulate load throughout the water column, as supported by the time-evolving erosion-deposition pattern and backscatter intensity.

The potential for more frequent moderate-level winter storms, predicted as result of future regional climatic changes exacerbated by human activities, could result in short-term (e.g., tidal phase) and long-term (e.g., seasonal) impacts in the form of more regular formation of a TMZ-style sedimentary flow dynamics in MTEs like those observed in the MR estuary in this study. A TMZ creates an aquatic environment that is known to stimulate flocculation, and greatly alters sediment settling dynamics, transport, and mass fluxes. More frequent TMZ formation in the MR and in other MTEs emptying into the Adriatic Sea would result in more frequent concentrated benthic suspension and fluid mud layers forming. Similar conclusions could be drawn for any MTEs globally that may experience similar seasonal and episodic changes in estuarine circulation in the future. The possible consequences are: longer net

sedimentary particle residence time (i.e. the time spent by sediments within the estuary); enhanced nearbed turbulence damping and drag reduction effects; more frequent, pulsed, bulk export events; effects on nautical depth; greater contaminant retention.

CRediT authorship contribution statement

Matteo Postacchini: Writing – review & editing, Writing – original draft, Visualization, Methodology, Investigation, Formal analysis, Data curation. **Andrew J. Manning:** Writing – review & editing, Writing – original draft, Software, Methodology, Formal analysis, Data curation, Conceptualization. **Joseph Calantoni:** Writing – review & editing, Writing – original draft, Resources, Methodology, Investigation, Funding acquisition, Formal analysis, Conceptualization. **Joseph P. Smith:** Writing – review & editing, Writing – original draft, Investigation, Funding acquisition, Data curation. **Maurizio Brocchini:** Writing – review & editing, Supervision, Resources, Methodology, Investigation, Funding acquisition, Conceptualization.

Declaration of competing interest

The authors declare the following financial interests/personal relationships which may be considered as potential competing interests: Maurizio Brocchini reports financial support was provided by Office of Naval Research Global. Maurizio Brocchini reports financial support was provided by Government of Italy Ministry of Education University and Research. Andrew J. Manning reports financial support was provided by US National Science Foundation. Joseph Calantoni reports financial support was provided by Office of Naval Research. Maurizio Brocchini reports a relationship with Gestiport spa that includes: consulting or advisory.

Data availability

Data will be made available on request.

Acknowledgments

The financial support from the Office of Naval Research Global (UK) MORSE Project (Research Grant N62909-17-1-2148) and the MIUR PRIN 2017 Project, Italy "FUNdamentals of BREAKing wave-induced boundary dynamics – FUNBREAK" (Grant Number 20172B7MY9) is gratefully acknowledged. AJM's contribution towards this research was partly supported by the US National Science Foundation under grants OCE-1736668 and OCE-1924532, TKI-MUSA project 11204950-000-ZKS-0002, and HR Wallingford company research FineScale project (ACK3013_62). J. C. was supported under base funding to the U.S. Naval Research Laboratory from the Office of Naval Research. We thank our colleagues who made significant contributions during the planning and execution of the field experiment including Edward F. Braithwaite III, Alex Sheremet, Allen Reed, Michael Fuller, Kevin Lois. Additionally, we thank the following authorities: the Municipality of Senigallia, the Capitaneria di Porto of Senigallia and of Ancona, MARIDIPART La Spezia and MARIFARI Venezia. Acknowledgments go also to: GESTIPORT (Senigallia), Club Nautico (Senigallia), NOTA srl (Senigallia), Carmar Sub (Ancona), Sena Gallica (Senigallia), METIS S.R.L. (Senigallia).

Appendix A. Hydrodynamic data

A.1 Longitudinal velocity during the small storm

A close-up view of the vertical profile of the longitudinal velocities is illustrated in Figure A. 1. The velocity profiles represent the longitudinal velocity contribution on 28/01/2014, between 07:00 and 21:00, with time step of 1 h. It is worth noting that the sediment deposition exists when the classical seawater-intrusion pattern establishes, while erosion occurs when the sea wave forcing dominates over the river flow, i.e. between ~10:00 and ~20:00.

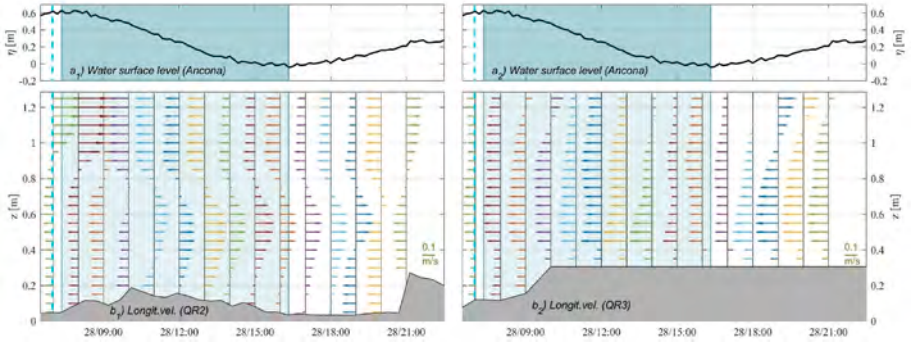

Fig. A. 1. Data collected during the SS. a) Water surface level at the tide gauge (Ancona). b)Longitudinal velocity component on 28/01/2014 (between 07:00 and 21:00, every hour). The location of the bed estimated from hourly averages of the pencil beam sonar line scans is overlaid in grey. Shaded areas highlight the period during which ebb tide occurred.

A.2 Analysis of water elevations at river quadpod locations

The comparison between tide-gauge signal and time-averaged water level at QR2 and QR3 shows an increase of the water elevation at the MR site in the end of the SS and a negligible sinking for both quadpods (Figure A. 2), this reinforcing the theory that the material on the quadpod feet was deposited sediment and not local sediment.

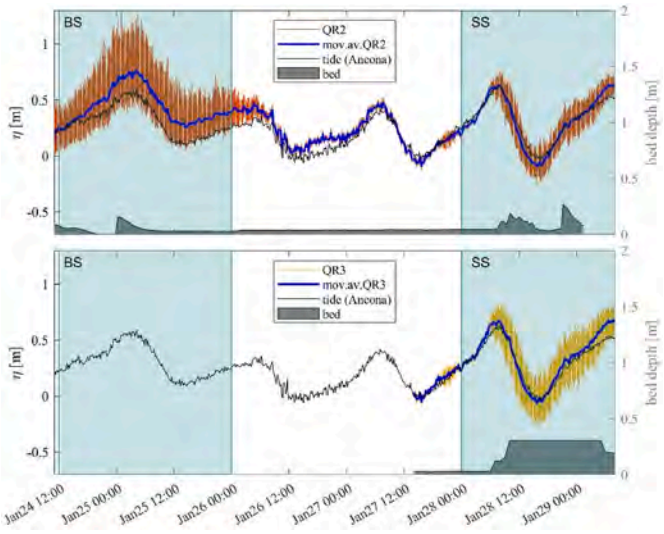

Fig. A. 2. Comparison of tide-gauge signal (black lines) with instantaneous (colored lines) and time-averaged (blue lines) water-surface elevation at QR2 (top) and QR3 (bottom). The bed level is reported as a grey area, while shaded areas highlight times during which BS and SS occurred.

Appendix B. Outline of empirical Flocculation Model

B.1 Outline of empirical Flocculation Model

The Flocculation Model (FM) for settling velocity (Ws) utilized in this paper is based entirely on empirical observations (200+ floc population data sets) made using non-intrusive floc and turbulence data acquisition techniques representative of a wide range of typical coastal and estuarine conditions. The FM comprises a series of algorithms representative of suspensions comprising pure mud and through to various combinations of mud:sand mixtures.

B.1.1 Floc Data for Algorithm Generation

Data comprised both in-situ field measurements and laboratory simulations. Approximately 200 individually observed floc populations were utilized spanning a wide range of suspended particulate matter (SPM) concentration and turbulence conditions within aquatic environments (laboratory generated and in-situ).

The floc population size (D) and settling velocity spectra were sampled using the video-based INSSEV (Manning and Dyer, 2002) and LabSFLOC instruments (Manning, 2006; Manning et al., 2017).

B.1.2 Algorithm Development

The FM algorithms were generated to be representative of suspensions of pure mud through to varying degrees of mixed sediment in terms of the particulate mass and dual settling velocities, both of which vary in response to shear stress and SPM concentration changes. Details of the FM algorithm derivations and preliminary testing of the floc settling algorithms are described by Manning and Dyer (2007), Manning (2008), and Manning et al. (2011).

A parametric multiple regression technique was chosen to analyze the various empirical data matrices and generate statistical relationships from the experimental data. The aim was to separate the field of varying SPM concentration and τ empirical results, by curves representative of a number of parameter ranges. For the multiple regression, the following floc/aggregate characteristics were considered the most important and relevant: macrofloc settling velocity (Ws_{MACRO}), microfloc settling velocity (Ws_{micro}), total SPM concentration (SPM), percentage of SPM constituting the macrofloc portion of a floc population (SPM_{MACRO}), percentage of SPM constituting the microfloc portion of a floc population (SPM_{micro}), turbulent shear stress parameter derived from turbulence kinetic energy (τ).

The FM algorithms are based on the segregation of flocs into macroflocs (D > 160 μm) and microflocs (D < 160 μm), which comprise the constituent particles of the macroflocs. This distinction permits the discrete computation of the mass settling flux (MSF) at any point in a coastal and estuarine water column. Equations are given for (Manning, 2004): i) the settling velocity of the macrofloc fraction; ii) the settling velocity of microflocs; iii) the ratio of macrofloc mass to microfloc mass in each floc population (SPM_{ratio}). These equations require the input of a turbulent shear stress (τ) and an SPM concentration.

B.2 Results of the Flocculation Model

Table A.1, Table A.2 and Table A.3 summarize both input parameters and outputs of the FM (see Sections 2.3 and 3.4) relevant to scenarios 1, 2 and 3, respectively. The illustrated data refer to an elevation of 0.25 m above the bed.

Table A.1
FM outputs for scenario 1 (SS): floc characteristics 0.25 m above bed.

Dist. from mouth [km]	Mud [%]	Sand [%]	Turbidity [NTU]	SSC [mg/l]	Ws_{macro} (0.06Pa) [mm/s]	Ws_{macro} (0.35Pa) [mm/s]	Ws_{macro} (0.6Pa) [mm/s]	Ws_{macro} (0.9Pa) [mm/s]	Ws_{micro} (0.06Pa) [mm/s]	Ws_{micro} (0.35Pa) [mm/s]	Ws_{micro} (0.6Pa) [mm/s]	Ws_{micro} (0.9Pa) [mm/s]	SPM_{ratio}	MSF (0.06Pa) [mg. $m^{-2}s^{-1}$]	MSF (0.35Pa) [mg. $m^{-2}s^{-1}$]	MSF (0.6Pa) [mg. $m^{-2}s^{-1}$]	MSF (0.9Pa) [mg. $m^{-2}s^{-1}$]
−0.475	100	0	250	2500	2.34	3.49	2.70	1.96	0.43	0.93	0.86	0.69	7.89	5303	8010	6229	4543
−0.475	75	25	250	2500	1.98	4.15	2.79	1.98	0.97	0.97	1.41	1.85	2.16	4151	7849	5887	4848
+0.025	50	50	155	1550	1.22	2.79	3.11	1.38	1.17	2.24	2.51	2.19	0.84	1852	3854	4313	2824
+0.525	0	100	65	650	6.80	6.80	6.80	6.80	6.80	6.80	6.80	6.80	1.00	4420	4420	4420	4420

Table A.2
FM outputs for scenario 2 (BS): floc characteristics 0.25 m above bed.

Dist. from mouth [km]	Mud [%]	Sand [%]	Turbidity [NTU]	SSC [mg/l]	Ws_{macro} (0.06Pa) [mm/s]	Ws_{macro} (0.35Pa) [mm/s]	Ws_{macro} (0.6Pa) [mm/s]	Ws_{macro} (0.9Pa) [mm/s]	Ws_{micro} (0.06Pa) [mm/s]	Ws_{micro} (0.35Pa) [mm/s]	Ws_{micro} (0.6Pa) [mm/s]	Ws_{micro} (0.9Pa) [mm/s]	SPM_{ratio}	MSF (0.06Pa) [mg. $m^{-2}s^{-1}$]	MSF (0.35Pa) [mg. $m^{-2}s^{-1}$]	MSF (0.6Pa) [mg. $m^{-2}s^{-1}$]	MSF (0.9Pa) [mg. $m^{-2}s^{-1}$]
−0.475	100	0	130	1300	1.77	2.93	2.21	1.55	0.43	0.93	0.86	0.69	4.71	1996	3351	2563	1814
−0.475	75	25	130	1300	1.02	3.19	1.96	1.28	0.69	0.69	1.12	1.55	1.41	1148	2795	2097	1809
+0.025	50	50	80	800	0.83	2.39	2.55	1.05	1.03	2.10	2.38	2.07	0.62	763	1768	1956	1341
+0.525	0	100	40	400	6.80	6.80	6.80	6.80	6.80	6.80	6.80	6.80	1.00	2720	2720	2720	2720

Table A.3
FM outputs for scenario 3 (transition): floc characteristics 0.25 m above bed.

Dist. from mouth [km]	Mud [%]	Sand [%]	Turbidity [NTU]	SSC [mg/l]	Ws_{macro} (0.06Pa) [mm/s]	Ws_{macro} (0.35Pa) [mm/s]	Ws_{macro} (0.6Pa) [mm/s]	Ws_{macro} (0.9Pa) [mm/s]	Ws_{micro} (0.06Pa) [mm/s]	Ws_{micro} (0.35Pa) [mm/s]	Ws_{micro} (0.6Pa) [mm/s]	Ws_{micro} (0.9Pa) [mm/s]	SPM_{ratio}	MSF (0.06Pa) [mg. $m^{-2}s^{-1}$]	MSF (0.35Pa) [mg. $m^{-2}s^{-1}$]	MSF (0.6Pa) [mg. $m^{-2}s^{-1}$]	MSF (0.9Pa) [mg. $m^{-2}s^{-1}$]
−0.475	100	0	100	1000	1.63	2.79	2.09	1.44	0.43	0.93	0.86	0.69	3.86	1381	2403	1833	1286
−0.475	75	25	100	1000	0.78	2.95	1.76	1.10	0.61	0.61	1.05	1.48	1.19	707	1884	1432	1273
+0.025	50	50	65	650	0.75	2.31	2.43	0.98	1.00	2.07	2.36	2.05	0.58	592	1403	1550	1076
+0.525	0	100	25	250	6.80	6.80	6.80	6.80	6.80	6.80	6.80	6.80	1.00	1700	1700	1700	1700

References

Allen, G.P., Salomon, J.C., Bassoullet, P., Du Penhoat, Y., De Grandpre, C., 1980. Effects of tides on mixing and suspended sediment transport in macrotidal estuaries. Sediment. Geol. 26 (1–3), 69–90.

Anthony, E.J., 2015. Wave influence in the construction, shaping and destruction of river deltas: a review. Mar. Geol. 361, 53–78.

Bagherimiyab, F., Lemmin, U., 2013. Shear velocity estimates in rough-bed open-channel flow. Earth Surf. Process. Landforms 38 (14), 1714–1724.

Baldoni, A., Perugini, E., Soldini, L., Calantoni, J., Brocchini, M., 2021. Long-term evolution of an inner bar at the mouth of a microtidal river. Estuar. Coast Shelf Sci. 262, 107573.

Bertin, X., Olabarrieta, M., 2016. Relevance of infragravity waves in a wave-dominated inlet. J. Geophys. Res.: Oceans 121 (8), 5418–5435.

Best, J.L., Leeder, M.R., 1993. Drag reduction in turbulent muddy seawater flows and some sedimentary consequences. Sedimentology 40 (6), 1129–1137.

Brocchini, M., 2020. Wave-forced dynamics in the nearshore river mouths, and swash zones. Earth Surf. Process. Landforms 45 (1), 75–95.

Brocchini, M., Calantoni, J., Reed, A.H., Postacchini, M., Lorenzoni, C., Russo, A., Mancinelli, A., Corvaro, S., Moriconi, G., Soldini, L., 2015. Summertime conditions of a muddy estuarine environment: the EsCoSed project contribution. Water Sci. Technol. 71 (10), 1451–1457.

Brocchini, M., Calantoni, J., Postacchini, M., Sheremet, A., Staples, T., Smith, J., Reed, A. H., BraithwaiteIII, E.F., Lorenzoni, C., Russo, A., Corvaro, S., Mancinelli, A., Soldini, L., 2017. Comparison between the wintertime and summertime dynamics of the Misa River estuary. Mar. Geol. 385, 27–40.

Burchard, H., Schuttelaars, H.M., Ralston, D.K., 2018. Sediment trapping in estuaries. Ann. Rev. Mar. Sci 10, 371–395.

Chen, N., Krom, M.D., Wu, Y., Yu, D., Hong, H., 2018. Storm induced estuarine turbidity maxima and controls on nutrient fluxes across river-estuary-coast continuum. Sci. Total Environ. 628, 1108–1120.

Colantoni, P., Mencucci, D., 2010. Some remarks on sediment dispersion in the Central-western Adriatic continental shelf. Geology of the Adriatic Area. GeoActa 57–87.

Cooper, J.A.G., 2001. Geomorphological variability among microtidal estuaries from the wave-dominated South African coast. Geomorphology 40 (1–2), 99–122.

Darvini, G., Memmola, F., 2020. Assessment of the impact of climate variability and human activities on the runoff in five catchments of the Adriatic Coast of south-central Italy. J. Hydrol.: Reg. Stud. 31, 100712.

Davies, J.L., 1964. A morphogenic approach to world shorelines. Zeitschrift fur Geomorphologie 8, 127–142.

De Moustier, C., Kraft, B.J., 2013. In situ beam pattern estimation from seafloor acoustic backscatter measured with swath mapping sonars. In: Proceedings of Meetings on Acoustics, 19. https://doi.org/10.1121/1.4800560, 1.

Dyer, K., 1986. Coastal and Estuarine Sediment Dynamics. John Wiley and Sons, Chichester, Sussex(UK), p. 358, 1986.

Dyer, K.R., 1989. Sediment processes in estuaries: future research requirements. J. Geophys. Res.: Oceans 94 (C10), 14327–14339.

Dyer, K.R., Bale, A.J., Christie, M.C., Feates, N., Jones, S., Manning, A.J., 2002. The turbidity maximum in a mesotidal estuary, the Tamar Estuary, UK: I. Dynamics of suspended sediment. In: Proceedings in Marine Science, vol. 5. Elsevier, pp. 203–218.

Dyer, K.R., Christie, M.C., Manning, A.J., 2004. The effects of suspended sediment on turbulence within an estuarine turbidity maximum. Estuar. Coast Shelf Sci. 59 (2), 237–248.

Eisma, D., 1986. Flocculation and de-flocculation of suspended matter in estuaries. Neth. J. Sea Res. 20 (2–3), 183–199.

Fain, A.M.V., Ogston, A.S., Sternberg, R.W., 2007. Sediment transport event analysis on the western Adriatic continental shelf. Continent. Shelf Res. 27 (3–4), 431–451.

Frignani, M., Langone, L., Ravaioli, M., Sorgente, D., Alvisi, F., Albertazzi, S., 2005. Fine-sediment mass balance in the western Adriatic continental shelf over a century time scale. Mar. Geol. 222, 113–133.

Geyer, W.R., Woodruff, J.D., Traykovski, P., 2001. Sediment transport and trapping in the Hudson River estuary. Estuaries 24 (5), 670–679.

Geyer, W.R., MacCready, P., 2014. The estuarine circulation. Annu. Rev. Fluid Mech. 46, 175–197.

Gill, A.E., 1982. Atmosphere-ocean Dynamics International Geophysics Series, vol. 30. Academic Press, US:California, p. 645.

Gratiot, N., Manning, A.J., 2008. Flocculation processes in concentrated benthic suspension layer (CBS) using a laboratory diffusive turbulent grid tank. In: Kudusa, T., Yamanishi, H., Spearman, J., Gailani, J.Z. (Eds.), Sediment and Ecohydraulics -Proc, Marine Science, vol. 9. Elsevier, Amsterdam, ISBN 978-0-444-53184-1, pp. 53–68.

Hansen, D.V., Rattray Jr., M., 1965. Gravitational circulation in straits and estuaries. J. Mar. Res. 23, 104–122.

Horemans, D.M., Dijkstra, Y.M., Schuttelaars, H.M., Meire, P., Cox, T.J., 2020. Unraveling the essential effects of flocculation on large-scale sediment transport patterns in a tide-dominated estuary. J. Phys. Oceanogr. 50 (7), 1957–1981.

Kennish, M.J., 2019. Ecology of Estuaries:. In: Physical and Chemical Aspects, 1 CRC press.

Kirby, R., Parker, W.R., 1982. A suspended sediment front in the Severn Estuary. Nature 295 (5848), 396–399.

Klammler, H., Penko, A.M., Staples, T., Sheremet, A., Calantoni, J., 2021. Observations and modeling of wave-induced burial and sediment entrainment: likely importance of degree of liquefaction. J. Geophys. Res.: Oceans 126 (8), e2021JC017378.

Krvavica, N., Gotovac, H., Lončar, G., 2021. Salt-wedge dynamics in microtidal Neretva River estuary. Reg. Stud. Mar. Sci. 43, 101713.

Krvavica, N., Travaš, V., Ožanić, N., 2016. A field study of interfacial friction and entrainment in a microtidal salt-wedge estuary. Environ. Fluid Mech. 16 (6), 1223–1246.
Krone, R.B., 1963. A study of rheological properties of estuarial sediments. In: Hyd. Eng. Lab. And Sanitary Eng. Lab. University of California, Berkeley, pp. 63–68.
Li, C., O'Donnell, J., 2005. The effect of channel length on the residual circulation in tidally dominated channels. J. Phys. Oceanogr. 35 (10), 1826–1840.
Lin, J., Kuo, A.Y., 2001. Secondary turbidity maximum in a partially mixed microtidal estuary. Estuaries 24 (5), 707–720.
Liungman, O., Rydberg, L., Göransson, C.G., 2001. Modeling and observations of deep water renewal and entrainment in a Swedish sill fjord. J. Phys. Oceanogr. 31 (12), 3401–3420.
Manning, A.J., 2004. Observations of the properties of flocculated cohesive sediment in three western European estuaries. J. Coast. Res. 41, 70–81. SI.
Manning, A.J., 2006. LabSFLOC – A Laboratory System to Determine the Spectral Characteristics of Flocculating Cohesive Sediments. HR Wallingford Technical Report. TR 156.
Manning, A.J., 2008. The development of algorithms to parameterize the mass settling flux of flocculated estuarine sediments. In: Kudusa, T., Yamanishi, H., Spearman, J., Gailani, J.Z. (Eds.), Sediment and Ecohydraulics -Proc, Marine Science, vol. 9. Elsevier, Amsterdam, ISBN 978-0-444-53184-1, pp. 193–210.
Manning, A.J., Bass, S.J., 2006. Variability in cohesive sediment settling fluxes: observations under different estuarine tidal conditions. Mar. Geol. 235 (1–4), 177–192.
Manning, A.J., Bass, S.J., Dyer, K.R., 2006. Floc properties in the turbidity maximum of a mesotidal estuary during neap and spring tidal conditions. Mar. Geol. 235 (1–4), 193–211.
Manning, A.J., Baugh, J.V., Spearman, J.R., Pidduck, E.L., Whitehouse, R.J.S., 2011. The settling dynamics of flocculating mud:sand mixtures: Part 1 – empirical algorithm development. In: Ocean Dynamics, INTERCOH 2009 special issue. https://doi.org/10.1007/s10236-011-0394-7.
Manning, A.J., Dyer, K.R., 2002. The use of optics for the in situ determination of flocculated mud characteristics. J. Opt. Pure Appl. Opt. 4 (4), S71.
Manning, A.J., Dyer, K.R., 2007. Mass settling flux of fine sediments in Northern European estuaries: measurements and predictions. Mar. Geol. 245, 107–122. https://doi.org/10.1016/j.margeo.2007.07.005.
Manning, A.J., Langston, W.J., Jonas, P.J.C., 2010. A review of sediment dynamics in the Severn Estuary: influence of flocculation. Mar. Pollut. Bull. 61 (1–3), 37–51.
Manning, A.J., Whitehouse, R.J.S., Uncles, R.J., 2017. Suspended particulate matter: the measurements of flocs. In: ECSA Practical Handbooks on Survey and Analysis Methods: Estuarine and Coastal Hydrography and Sedimentology, pp. 211–260.
Mehta, A.J., 2013. An Introduction to Hydraulics of Fine Sediment Transport, vol. 38. World Scientific Publishing Company.
Mehta, A.J., Lott, J.W., 1987. Sorting of fine sediment during deposition. In: Coastal Sediments. ASCE, pp. 348–362.
Melito, L., Postacchini, M., Darvini, G., Brocchini, M., 2018. Waves and currents at a river mouth: the role of macrovortices, sub-grid turbulence and seabed friction. Water 10 (5), 550.
Melito, L., Postacchini, M., Sheremet, A., Calantoni, J., Zitti, G., Darvini, G., Penna, P., Brocchini, M., 2020. Hydrodynamics at a microtidal inlet: analysis of propagation of the main wave components. Estuar. Coast Shelf Sci., 106603
Milliman, J.D., Syvitski, J.P., 1992. Geomorphic/tectonic control of sediment discharge to the ocean: the importance of small mountainous rivers. J. Geol. 100 (5), 525–544.
Monbet, Y., 1992. Control of phytoplankton biomass in estuaries: a comparative analysis of microtidal and macrotidal estuaries. Estuaries 15 (4), 563–571.
Niedda, M., Greppi, M., 2007. Tidal, seiche and wind dynamics in a small lagoon in the Mediterranean Sea. Estuar. Coast Shelf Sci. 74 (1–2), 21–30.
Nunes-Vaz, R.A., Lennon, G.W., Bowers, D.G., 1990. Physical behaviour of a large, negative or inverse estuary. Continent. Shelf Res. 10 (3), 277–304.
Orlic, M., Gacic, M., Laviolette, P.E., 1992. The currents and circulation of the Adriatic Sea. Oceanol. Acta 15 (2), 109–124.
Pawlowicz, R., Beardsley, B., Lentz, S., 2002. Classical tidal harmonic analysis including error estimates in MATLAB using T_TIDE. Comput. Geosci. 28 (8), 929–937.
Postacchini, M., Melito, L., Sheremet, A., Calantoni, J., Darvini, G., Corvaro, S., Brocchini, M., 2020. Upstream propagating long-wave modes at a microtidal river mouth. In: Environmental Sciences Proceedings, vol. 2. Multidisciplinary Digital Publishing Institute, p. 15, 1.
Postacchini, M., Darvini, G., Perugini, E., Martinelli, J., Ilari, M., Brocchini, M., 2022. Upriver propagation of tidal waves and mouth bar influence at a microtidal estuary: observations and modeling. In: 39th IAHR World Congress 2022: from Snow to Sea. IAHR.
Postma, H., 1980. Chemistry and Biogeochemistry of Estuaries.
Prandle, D., 2009. Estuaries: Dynamics, Mixing, Sedimentation and Morphology. Cambridge University Press.
Pritchard, D.W., 1967. What Is an Estuary: Physical Viewpoint. American Association for the Advancement of Science.
Restrepo, J.C., Schrottke, K., Traini, C., Bartholomae, A., Ospino, S., Ortíz, J.C., et al., 2018. Estuarine and sediment dynamics in a microtidal tropical estuary of high fluvial discharge: magdalena River (Colombia, South America). Mar. Geol. 398, 86–98.
Ross, M.A., Mehta, A.J., 1989. On the mechanics of lutoclines and fluid mud. J. Coast Res. 51–62.
Schubel, J.R., 1968. Turbidity maximum of the northern Chesapeake Bay. Science 161 (3845), 1013–1015.
Soulsby, R.L., Manning, A.J., Spearman, J., Whitehouse, R.J.S., 2013. Settling velocity and mass settling flux of flocculated estuarine sediments. Mar. Geol. https://doi.org/10.1016/j.margeo.2013.04.006.
Souto, C., Gilcoto, M., Fariña-Busto, L., Pérez, F.F., 2003. Modeling the residual circulation of a coastal embayment affected by wind-driven upwelling: circulation of the Ría de Vigo (NW Spain). J. Geophys. Res.: Oceans 108 (C11).
Spearman, J., Manning, A.J., 2008. On the significance of mud transport algorithms for the modelling of intertidal flats. In: Kudusa, T., Yamanishi, H., Spearman, J., Gailani, J.Z. (Eds.), Sediment and Ecohydrauli–S - Proc, Marine Science, vol. 9. Elsevier, Amsterdam, ISBN 978-0-444-53184-1, pp. 411–430.
Spencer, K.L., Manning, A.J., Droppo, I.G., Leppard, G.G., Benson, T., 2010. Dynamic interactions between cohesive sediment tracers and natural mud. J. Soils Sediments 10 (7). https://doi.org/10.1007/s11368-010-0291-6.
Stommel, H., Farmer, H.G., 1953. Control of salinity in an estuary by a transition. J. Mar. Res. 12 (1), 13–20.
Talke, S.A., de Swart, H.E., De Jonge, V.N., 2009. An idealized model and systematic process study of oxygen depletion in highly turbid estuaries. Estuar. Coast 32 (4), 602–620.
Tambo, N., Watanabe, Y., 1979. Physical characteristics of flocs—I. The floc density function and aluminium floc. Water Res. 13 (5), 409–419.
Tomadin, L., 2000. Sedimentary fluxes and different dispersion mechanisms of the clay sediments in the Adriatic Basin. Rendiconti Lincei 11 (3), 161–174.
Uncles, R.J., Elliott, R.C.A., Weston, S.A., 1985. Observed fluxes of water, salt and suspended sediment in a partly mixed estuary. Estuar. Coast Shelf Sci. 20 (2), 147–167.
Uncles, R.J., Joint, I., Stephens, J.A., 1998. Transport and retention of suspended particulate matter and bacteria in the Humber-Ouse Estuary, United Kingdom, and their relationship to hypoxia and anoxia. Estuaries 21 (4), 597–612.
Uncles, R.J., Stephens, J.A., Smith, R.E., 2002. The dependence of estuarine turbidity on tidal intrusion length, tidal range and residence time. Continent. Shelf Res. 22 (11–13), 1835–1856.
Valle-Levinson, A. (Ed.), 2010. Contemporary Issues in Estuarine Physics. Cambridge University Press.
Whitehouse, R.J.S., Soulsby, R., Roberts, W., Mitchener, H.J., 2000. Dynamics of Estuarine Muds. Thomas Telford Publications, London.
Wijeratne, E.M.S., Rydberg, L., 2007. Modelling and observations of tidal wave propagation, circulation and residence times in Puttalam Lagoon, Sri Lanka. Estuar. Coast Shelf Sci. 74 (4), 697–708.
Winterwerp, J.C., Van Kesteren, W.G., 2004. Introduction to the Physics of Cohesive Sediment Dynamics in the Marine Environment. Elsevier.
Wolanski, E., Chappell, J., Ridd, P., Vertessy, R., 1988. Fluidization of mud in estuaries. J. Geophys. Res.: Oceans 93 (C3), 2351–2361.
Zhang, N., Thompson, C.E.L., Townend, I.H., Rankin, K.E., Paterson, D.M., Manning, A. J., 2018. Nondestructive 3D imaging and quantification of hydrated biofilm-sediment aggregates using X-ray microcomputed tomography. Environ. Sci. Technol. 52, 13306–13313. https://doi.org/10.1021/acs.est.8b03997.